RESEARCH ARTICLE

Correspondence to:
J. Chen,
j.chen3@uu.nl

Vaporization of fault water during seismic slip

Jianye Chen[1,2] iD, André R. Niemeijer[1] iD, and Peter A. Fokker[1,3]

[1]HPT Laboratory, Department of Earth Sciences, Utrecht University, Utrecht, Netherlands, [2]State Key Laboratory of Earthquake Dynamics, Institute of Geology, China Earthquake Administration, Beijing, China, [3]TNO Applied Geosciences, Utrecht, Netherlands

Abstract Laboratory and numerical studies, as well as field observations, indicate that phase transitions of pore water might be an important process in large earthquakes. We present a model of the thermo-hydro-chemo-mechanical processes, including a two-phase mixture model to incorporate the phase transitions of pore water, occurring during fast slip (i.e., a natural earthquake) in order to investigate the effects of vaporization on the coseismic slip. Using parameters from typical natural faults, our modeling shows that vaporization can indeed occur at the shallow depths of an earthquake, irrespective of the wide variability of the parameters involved (sliding velocity, friction coefficient, gouge permeability and porosity, and shear-induced dilatancy). Due to the fast kinetics, water vaporization can cause a rapid slip weakening even when the hydrological conditions of the fault zone are not favorable for thermal pressurization, e.g., when permeability is high. At the same time, the latent heat associated with the phase transition causes the temperature rise in the slip zone to be buffered. Our parametric analyses reveal that the amount of frictional work is the principal factor controlling the onset and activity of vaporization and that it can easily be achieved in earthquakes. Our study shows that coseismic pore fluid vaporization might have played important roles at shallow depths of large earthquakes by enhancing slip weakening and buffering the temperature rise. The combined effects may provide an alternative explanation for the fact that low-temperature anomalies were measured in the slip zones at shallow depths of large earthquakes.

1. Introduction

Experimental and numerical studies have shown that frictional weakening of fault gouges at high (seismic) slip rates is dramatic [e.g., *Rice*, 2006; *Di Toro et al.*, 2011]. Various slip-weakening mechanisms have been proposed and examined in experimental and theoretical studies, including melt lubrication [*Hirose and Shimamoto*, 2005; *Di Toro et al.*, 2005], flash heating [*Rice*, 2006; *Beeler et al.*, 2008; *Goldsby and Tullis*, 2011], silica gel formation [*Goldsby and Tullis*, 2002; *Di Toro et al.*, 2004], nanopowder lubrication [*Han et al.*, 2010; *Reches and Lockner*, 2010], thermal pressurization [*Lachenbruch*, 1980; *Noda and Shimamoto*, 2005; *Rice*, 2006], and thermochemical pressurization [*Hirose and Bystricky*, 2007; *Sulem and Famin*, 2009; *Brantut et al.*, 2010, 2011b; *De Paola et al.*, 2011] (see also *Niemeijer et al.* [2012] for a review). However, previous friction experiments at seismic slip rates were mostly performed at room humidity conditions. Technological challenges related to simultaneous confinement of the pore fluid and the powdered sample have severely hindered the detailed investigation of the role of water and pore pressure in the dynamic slip-weakening process [e.g., *Kitajima et al.*, 2010]. For those wet experiments which have been done on fault gouges derived from faults and landslides, thermal pressurization of the pore fluid was generally believed to be the dominant weakening mechanism [e.g., *Ferri et al.*, 2010; *Kitajima et al.*, 2010; *Boutareaud et al.*, 2010; *Togo et al.*, 2014], although the state of the pore water (liquid or gaseous) was unknown and consequently the role of the fluid state on the observed dynamic weakening remains poorly understood [*Mizoguchi et al.*, 2007b, 2009; *Boutareaud et al.*, 2010; *Ujiie and Tsutsumi*, 2010; *Kitajima et al.*, 2010; *Ferri et al.*, 2011; *Faulkner et al.*, 2011; *Ujiie et al.*, 2013].

At the same time, vapor pressurization has been suggested as an important slip-weakening mechanism in dry experiments on fault gouges containing abundant hydrated minerals [*Boutareaud et al.*, 2010; *Mizoguchi et al.*, 2009; *Ferri et al.*, 2010; *Ujiie and Tsutsumi*, 2010; *Kitajima et al.*, 2010; *Chen et al.*, 2013]. In these tests, dehydration of clay minerals was attained by temperature rise due to frictional heating, and the subsequent, pronounced slip weakening observed was suggested to be due to fluid pressurization associated with the vaporization of the dehydrated water. Evidence

supporting this process included observations of large amounts of fault-normal dilation [e.g., *Boutareaud et al.*, 2010], an increase in humidity measured in close proximity of the deforming gouge [*Ujiie and Tsutsumi*, 2010], and the presence of altered, dehydrated minerals in the deformed samples [e.g., *Ferri et al.*, 2011]. Additionally, in some tests, water vapor was directly observed to escape the sample assembly, past the Teflon sleeve, during the experiments [*Hirose and Bystricky*, 2007; *Mizoguchi et al.*, 2009; *Kitajima et al.*, 2011; *Chen et al.*, 2013]. On the basis of a detailed consideration of the energy budget involved in high-velocity friction (HVF) experiments, *Kitajima et al.* [2010] suggested that shear-induced vaporization might be a significant heat sink for the dynamic faulting process. *Brantut et al.* [2011b] performed HVF experiments on gypsum rock cylinders, which showed that the temperature of the sliding surface was efficiently buffered during the gypsum dehydration reaction. In particular, they found that the temperature close to the sliding surface was remarkably constant at 100°C for a duration of several meters of slip. This suggests that the water produced during the reaction undergoes an isothermal phase transition to vapor. We have recently performed experiments on water-saturated limestone fault gouges using a sample assembly, specially designed to simulate well-defined, constant fluid drainage conditions [*Chen et al.*, 2017]. The results show that upon vaporization, the pore pressures increase, while the temperatures in the gouge are buffered endothermically, such that the pore water moves along the liquid-vapor transition curve in the pressure-temperature phase diagram.

Shear-induced water vaporization has also been reported to have occurred in natural earthquakes. *Weatherley and Henley* [2013] proposed that fluid depressurization during earthquake slip leads to flash vaporization which would lead to precipitation of ore minerals. These authors argued that the widespread occurrence of gold deposits in fault zones provides evidence for the extensive operation of this mechanism. It has also been proposed that earthquake lights are due to the fluid phase transition that occurs in and near the active slip zone, since vaporization of pore water can cause a dramatic decrease in electrical conductivity of the shear zone and at the same time produce significant electric charge separation by the so-called "waterfall electrification" effect [*Lockner et al.*, 1983]. Flashes of light together with huge rock eruptions were observed at the Chiu-Fen-Erh-Shan area during the Chi-Chi earthquake and inferred to be due to vapor pressurization generated by frictional heating [*Huang et al.*, 2003]. In addition, water vaporization has also been held responsible for catastrophic large landslides, allowing the movement of a huge amount of land mass to great distances, even on low-angle sliding surfaces [*Habib*, 1975; *Anderson*, 1985; *Vardoulakis*, 2002].

Recently, a growing number of numerical studies have shown that thermal pressurization could be important in contributing to the dynamic slip weakening associated with large earthquakes, such as the 1999 Chi-Chi earthquake [*Tanikawa et al.*, 2009], the 2008 Wenchuan earthquake [*Chen et al.*, 2013], and the 2011 Tohoku-Oki earthquake [*Tanikawa et al.*, 2013]. As highlighted by these studies, the local pressure-temperature (PT) conditions inside the slip zone can vary over a large range during faulting [e.g., *Wibberley and Shimamoto*, 2005], which can potentially induce multiple phase changes of the pore water, from the liquid to supercritical states or to vapor gaseous form [*Sulem et al.*, 2007; *Tanikawa et al.*, 2009; *Brantut et al.*, 2010; *Chen et al.*, 2013]. As proposed by *Sulem et al.* [2007], shear heating can lead to vaporization of fluids in a fault during an earthquake, and propagation of large earthquakes into the shallow crust could be facilitated by this mechanism. However, none of the above mentioned modeling studies considered the phase transition of water.

The purpose of this paper is to present numerical model simulations incorporating the complex coupled multiphase fluid flow and heat transfer phenomena during seismic slip. In doing this, we extend previous models of thermal or thermochemical pressurization to include the phase transition of pore water from liquid to vapor caused by frictional heating (the derivation and verification of the proposed model are given in detail in the appendices). The main question that we address in this work is how important fluid vaporization is in dynamically weakening faults and how fault temperature evolves when vaporization is operating. Using parameters from typical earthquake faults such as the Chelungpu fault and the Yingxiu-Beichuan fault, our modeling results show that shear-induced vaporization can occur extensively at shallow levels of a fault during a large earthquake, irrespective of the wide variability of the parameters involved. Finally, we discuss the general implications of water vaporization for the propagation of natural earthquakes and buffering fault temperatures.
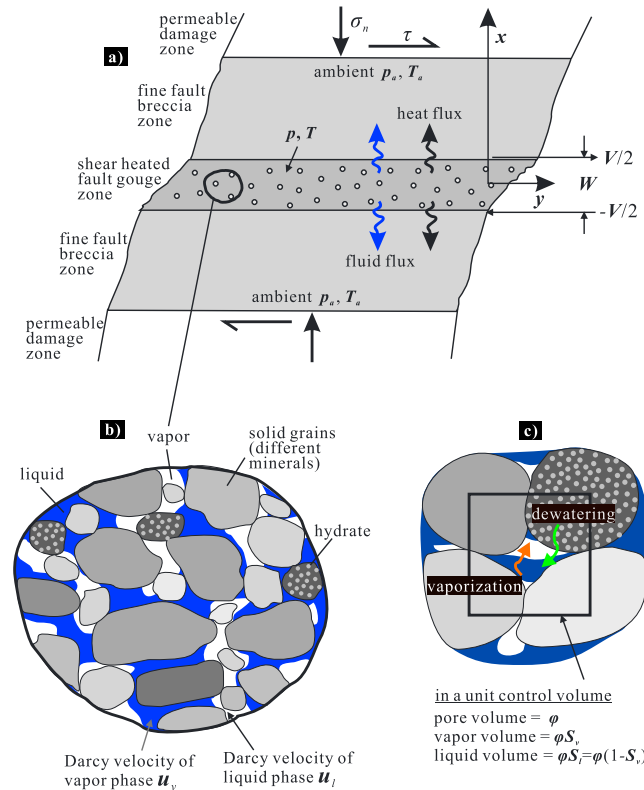
Figure 1. Sketch of the problem. (a) A fault zone consisting of a central gouge layer, adjacent fine breccia zones and outside permeable damage zone. The gouge layer of thickness W is subjected to a uniform or localized shear displacement at a constant rate V, and under a constant normal stress σ_n and a homogeneous shear stress τ. (b) A representative volume of the fault gouge containing a multiphase mixture. (c) Illustration of the dehydration and pore water vaporization in a unit control volume.

2. Problem Formulation

For the formulation of our problem, we consider a one-dimensional planar fault model as shown in Figure 1a, in which coseismic shear deformation is assumed to occur in a gouge zone of thickness W ($-W/2 < x < W/2$). Based on field studies of seismogenic faults [e.g., *Tanikawa et al.*, 2009; *Chen et al.*, 2013], we further assume that the gouge zone is bordered by a fault breccia zone of thickness greater than W and an outside damaged zone (Figure 1a). During an earthquake, frictional heat generated in the slip zone will induce a temperature rise and thus a pore pressure rise, as well as the possible activation of chemical reactions. Meanwhile, the pore water contained in the fault gouge may undergo an endothermic phase transition if the local temperature reaches the boiling temperature (Figures 1b and 1c). Upon pore water vaporization, the gouge will become a solid-liquid-vapor multiphase system, such that the previously proposed formulas for thermal pressurization (TP) or thermochemical pressurization (TCP) cannot apply

[*Lachenbruch*, 1980; *Noda and Shimamoto*, 2005; *Rice*, 2006; *Sulem and Famin*, 2009; *Brantut et al.*, 2010; *Tanikawa et al.*, 2009; *Chen et al.*, 2013]. New equations incorporating the phase transition are required.

2.1. Energy Conservation Equation for a Phase Transition Problem

Various forms of governing equations have been proposed to express the energy conservation of a multiphase porous media system, in which the thermal effect associated with a phase transition is expressed either in an "apparent heat capacity" or as a "heat source term" or even implicit by using enthalpy to express the energy balance [*Voller et al.*, 1990; *Lee and Tzong*, 1991; *Muhieddine et al.*, 2009]. To be consistent with the form usually used in modeling a fluid-pressurized faulting process [cf. *Rice*, 2006; *Sulem and Famin*, 2009; *Brantut et al.*, 2010], the source term method is employed in this study. As derived in Appendix A, the energy conservation equation governing a coseismic slip process, incorporating the phase transition of pore water, can be written as follows:

$$\rho_b c_b \frac{\partial T}{\partial t} = \frac{\partial}{\partial x}\left(K_b \frac{\partial T}{\partial x}\right) + Q_{\text{fr}} + Q_{\text{ch}} + Q_{\text{lv}} \tag{1}$$

In equation (1), T is temperature, t is time, and K_b, ρ_b, and c_b are thermal conductivity, density, and specific heat of the bulk sample, respectively; Q_{fr} is the heat source per unit volume generated by frictional heating, and Q_{ch} is the heat production per unit volume by chemical reactions (i.e., Q_{ch} is negative for endothermic reactions and positive for exothermic reactions). Further, the latent heat associated with an internal phase transition Q_{lv}, is "isolated" as a heat source, with a negative or a positive sign for a vaporization or a condensation process, respectively. Ignoring this term, equation (1) is identical to that previously proposed for TCP [e.g., *Sulem and Famin*, 2009; *Brantut et al.*, 2010; *Chen et al.*, 2013].

Table 1. Variables in the Two-Phase Mixture Model for Coseismic Vaporization

Variables for Mixture	Expressions	Reference
Density of bulk sample	$\rho_b = (1 - \varphi)\rho_s + \varphi\rho_f$	equation (A2b)
Enthalpy of bulk sample	$h_b = [(1 - \varphi)\rho_s h_s + \varphi\rho_f h_f]/\rho_b$	equation (A2b)
Thermal conductivity of bulk sample	$K_b = (1 - \varphi)K_s + \varphi K_f$	equation (A2b)
Specific heat of bulk sample	$c_b = [(1 - \varphi)\rho_s c_s + \varphi\rho_f c_f]/\rho_b$	equation (A4)
Density of pore fluid	$\rho_f = S_l\rho_l + S_v\rho_v$	equation (A2a)
Enthalpy of pore fluid	$h_f = (S_l\rho_l h_l + S_v\rho_v h_v)/\rho_f$	equation (A2a)
Thermal conductivity of pore fluid	$K_f = S_l K_l + S_v K_v$	equation (A2a)
Specific heat of pore fluid	$c_f = (S_l\rho_l c_l + S_v\rho_v c_v)/\rho_f$	equation (A4)
Compressibility of pore fluid	$\beta_f = S_v\beta_v + S_l\beta_l$	equation (B14)
Thermal expansivity of pore fluid	$\alpha_f = S_v\alpha_v + S_l\alpha_l$	equation (B14)
Kinematic viscosity of pore fluid	$v_f = 1/(k_{rl}/v_l + k_{rv}/v_v)$	*Shi and Wang* [2011]
Dynamic viscosity of pore fluid	$\eta_f = \rho_f/v_f$	equation (B15)
Relative permeability of pore fluid	$k_{rl} = S_l$ and $k_{rv} = S_v$	equation (B16)

However, when a vapor phase is present, the fault gouge becomes a three-phase mixture, and all the thermophysical properties, i.e., K_b, ρ_b, and c_b, become functions of the properties of its constituents (i.e., solid, liquid, and vapor phases, Table 1) and also of the vapor saturation, S_v, which denotes the volumetric fraction of the void space occupied by the vapor phase. It should be stressed that equation (1) is formulated based on the assumption of local thermodynamic equilibrium of the fault gouge, which means that the pore fluid is always at the same macrotemperature as the solids (see Appendix A for details). This assumption is plausible in the absence of a vapor phase since liquid water is thermally conductive such that the heat exchange between liquid water and solids is fast [*Wang and Beckermann*, 1993; *Wang*, 1997]. However, previous modeling work indicated that local thermal nonequilibrium is possible in the two-phase coexistent region of a granular material, and this effect cannot be neglected when the solid grains are large (>0.2 mm) [*Shi and Wang*, 2011]. Fortunately, particles in natural fault gouges are usually micron or submicron sized, especially in the principal slip zones associated with large earthquakes [e.g., *Ma et al.*, 2006].

Frictional work done by an earthquake is distributed among frictional heating, chemical reactions, phase transitions, grain deformation, and comminution [*Rice*, 2006]. In the absence of appropriate fracture energy data, only the first three processes are considered in our modeling.

1. Uniform shearing rate within a slip band is assumed, and the heat production rate is then given by

$$Q_{fr} = \tau\dot{\gamma} = \mu_d(\sigma_n - \overline{p})V/w, \qquad (2)$$

   where τ is shear stress, $\dot{\gamma}$ is shear strain rate, μ_d is dynamic friction coefficient, V is slip velocity, and w is the thickness of the slip band ($w \leq W$). Further, σ_n is normal stress and $\overline{p}$ is the mean pore pressure inside the slip band. Mechanical equilibrium is assumed so that the variation of τ within a slip band can be neglected [*Sulem et al.*, 2007]. The shear resistance is thus taken to be proportional to the mean effective normal stress ($\sigma_n - \overline{p}$) inside the slip zone [*Sulem et al.*, 2007; *Brantut et al.*, 2010]. The frictional heating will stop when $\overline{p}$ overshoots the normal stress acting on the fault plane ($\overline{p} > \sigma_n$).

2. The heat produced or consumed by chemical reactions is expressed as

$$Q_{ch} = \Sigma \frac{\rho_s(1 - \varphi)\omega_i}{M_i}\Delta H_i \frac{\partial\xi_i}{\partial t}, \qquad (3)$$

   Here Σ represents the summation of all involved reactions. The term ΔH_i represents the molar enthalpy change of the reaction (i) and is negative when endothermic so that heat is consumed, φ is the porosity, ω_i and M_i are the wt % content and molar mass of the reactant (i) contained in the solid grains in the fault gouge, and ρ_s is the density of the solid grains. Finally, ξ_i is the cumulative reacted mass fraction of the reactant (i) through time, and its time derivative $\partial\xi_i/\partial t$ expresses the reaction kinetics.

3. The thermal effect associated with the phase transition of water in the pore space can be calculated as

$$Q_{lv} = \varphi\rho_l \frac{\Delta H_{lv}}{M_{H_2O}} \frac{dS_v}{dt}. \qquad (4)$$
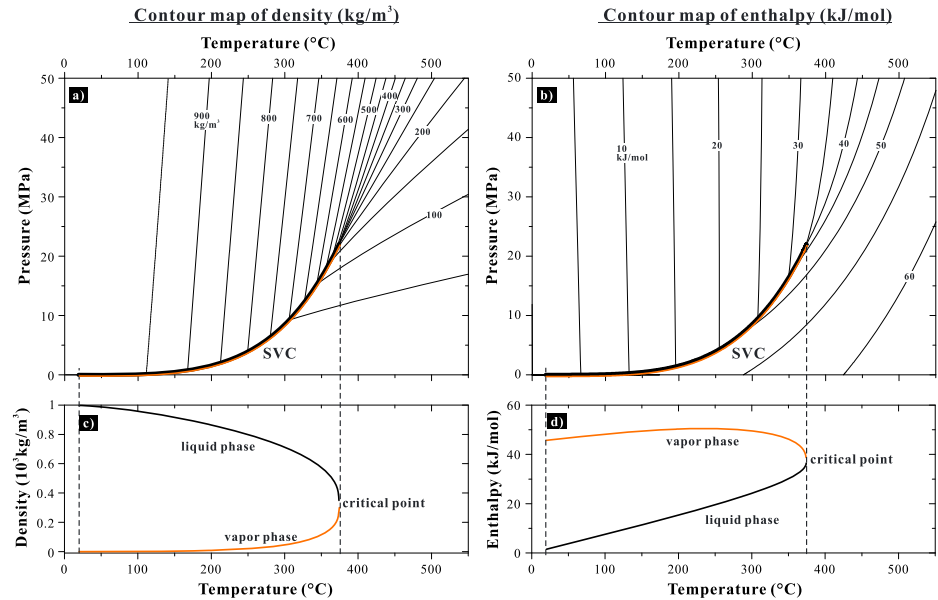
Figure 2. Contour map of (a) density and (b) enthalpy of water with respect to temperature and pressure. (c and d) The discontinuities in density and enthalpy along the saturated vapor curve (SVC) are shown. The large density and enthalpy differences between liquid and vapor phases of water indicate the potentially significant pressurization and endothermic effects associated with a liquid-to-vapor transition.

In expression (4), ρ_l is the density of liquid water, M_{H2O} is the molar mass of water, and ΔH_{lv} represents the enthalpy change associated with the "phase" transition of per molar water (J/mol). The variable S_v appearing in equation (4) is vapor saturation. Likewise, S_l is liquid saturation, denoting the relative volumetric fraction of the liquid phase in the pore space which yields $S_v + S_l = 1$. The time derivatives ($dS_v/dt = -dS_l/dt$) specify the phase transition rate. As a reversible process, a positive dS_v/dt indicates vaporization, while a negative value denotes condensation. Note that nonzero Q_{lv} is only possible when the PT conditions are below the critical point ($p = 22.06$ MPa, $T = 374°C$, Figure 2). In particular, as temperature (or pressure) increases, the enthalpy differences between liquid and vapor water, ΔH_{lv}, will get smaller and smaller and ultimately become zero upon approaching the critical point (Figures 2b and 2d). See Appendix A for a detailed derivation of the energy conservation equation.

2.2. Fluid Mass Conservation Equation for a Phase Transition Problem

As aforementioned, when a phase transition occurs, the shearing fault gouge becomes a multiphase system and the pore fluid trapped in the fault gouge will involve both vapor and liquid phases. To characterize this, a two-phase mixture model, following *Wang and Beckermann* [1993], was developed for the coseismic slip process (see detailed derivation in Appendix B). The fluid mass conservation including a shear-induced phase transition can be described as follows:

$$S_s \frac{\partial p}{\partial t} = \frac{\partial}{\partial x}\left(\frac{k}{\eta_f}\frac{\partial p}{\partial x}\right) + \Omega_T + \Omega_{ch} + \Omega_{lv} - \frac{d\varphi_d}{dt}. \tag{5}$$

In equation (5), p is pore pressure, and k and S_s are intrinsic permeability and specific storage of fault rocks, respectively. Further, η_f is the dynamic viscosity of the mixed-phase pore fluid; the terms Ω_T and Ω_{ch} and Ω_{lv} represent the fluid volume expansion or generation rates per unit volume fault rock by thermal pressurization, chemical reactions, and the phase transition, respectively (in unit of m³/(m³s)). Their values divided by S_s give the corresponding fluid pressurization rates (Pa/s). The last term $d\varphi_d/dt$ specifies the dilatancy rate. Since the capillary pressure due to interfacial forces, as estimated by $2\gamma/r$ (where γ is the interfacial tension of about 0.07 N/m, r is the effective radius of the interface which is in the order of the grain size, 10 μm), is much smaller than the pore pressure investigated in the present study, the fluid flow driven by capillary pressure is ignored in equation (5). Note that all the properties for a mixture fluid are functions of the properties of the liquid and vapor phase water (see section 3.1).

1. The fluid volume expansion rate caused by pure thermal expansion (TP) can be expressed as

$$\Omega_T = \varphi(\alpha_f - \alpha_s)\frac{\partial T}{\partial t},\qquad(6)$$

   where α_f and α_s are the thermal expansivities of the fluid and individual solid grains, respectively.

2. Besides thermal effects, some chemical reactions influence the evolution of the pore pressure by fluid mass production through dehydration or decarbonation. Reactions can also involve volume change in the solid phases. For example, dehydration of smectite can produce a solid volume reduction up to 47%. Such a reduction is associated with lattice collapse and is expected to yield an inelastic porosity increase in bulk rocks [*Wong et al.*, 1997]. Assuming 1 mol hydrate converts to 1 mol dehydrate, losing χ mol water and producing a volume reduction in solid phase ΔV, the effective fluid volume generation rate can be expressed as follows:

$$\Omega_{ch} = \Sigma(1-\varphi)\omega_i\Pi_i\frac{\partial\xi_i}{\partial t}.\qquad(7)$$

   Here $\Pi_i = \frac{\chi_i M_{H_2O}}{M_i}\frac{\rho_s}{\rho_l} - \Delta V_i$ is the net volume change of pore water that is caused by the reaction of a unit volume of reactant (*i*) (also referred to as the specific expelled water) [*Chen et al.*, 2013], where M_{H2O}/M_i is the ratio between the molar mass of water and reactant, ρ_l is the density of the pore fluid phase, and χ_i and ΔV_i are the water-containing index and specific solid volume shrinkage associated with the dehydration reaction. Positive ΔV_i value indicates volume loss in the solids. For a detailed derivation of Ω_{ch}, see Appendix B. Decarbonation reactions can be treated in a similar way [*Sulem and Famin*, 2009; *Chen et al.*, 2013].

3. When the temperature reaches the boiling temperature, pore water begins to vaporize. This process can have significant pressurization effects because the density of vapor water can be three orders of magnitude lower than that of liquid water in the same condition (Figures 2a and 2c). The fluid volume generation rate by vaporization can be expressed as follows:

$$\Omega_{lv} = \varphi\left(\frac{\rho_l}{\rho_v} - 1\right)\frac{dS_v}{dt}.\qquad(8)$$

   Here ρ_l and ρ_v are densities of liquid and vapor water, respectively. Similar to Q_{lv}, nonzero Ω_{lv} is possible only when the PT conditions are below the critical point. As temperature increases, the difference of densities between liquid and vapor water gets smaller (Figure 2c) and ultimately brings Ω_{lv} to zero upon reaching the critical point. Note again that a phase transition is a reversible process so that condensation (negative dS_v/dt) can lead to fluid depressurization.

4. Without the last two terms, equation (5) corresponds to a dilationless fault as considered by *Lachenbruch* [1980]. However, considering the fault surface irregularities and the increasing strain rate in a dynamic faulting process, shear-induced dilatancy is likely to occur under natural situations [*Marone et al.*, 1990; *Segall and Rice*, 1995]. The dilatancy rate can be written as $d\varphi_d/dt = \Delta\varphi_d\delta_d(t)$, where $\Delta\varphi_d$ is the pore suction caused by the dilatancy and $\delta_d(t)$ is the time function for dilatancy (its integral equals to unity). For simplicity, it is assumed here that all the dilatancy essentially takes place in the earliest stage of slip, with no further dilatancy as significant slip develops [*Garagash and Rudnicki*, 2003; *Rice*, 2006]. As such, the depressurization effect of shear-induced dilatancy can be taken into account through reducing the pore pressure by $\Delta\varphi_d/S_s$ [see also *Rice*, 2006]. For the duration of seismic slip that is simulated in this study, such a quasi-instantaneous change should be treated as an initial condition.

2.3. Chemical Reactions

Various chemical reactions have been reported to have occurred during rapid fault motion from both experiment and field observations, including dehydration, dehydroxylation, and transformation of clay minerals, decomposition of organic material, and of carbonates [e.g., *Ikehara et al.*, 2007; *Han et al.*, 2007]. The kinetics of chemical reactions is commonly expressed by relations of the form

$$\frac{\partial\xi_i}{\partial t} = f_i(\xi_i)\kappa_i(T),\qquad(9)$$
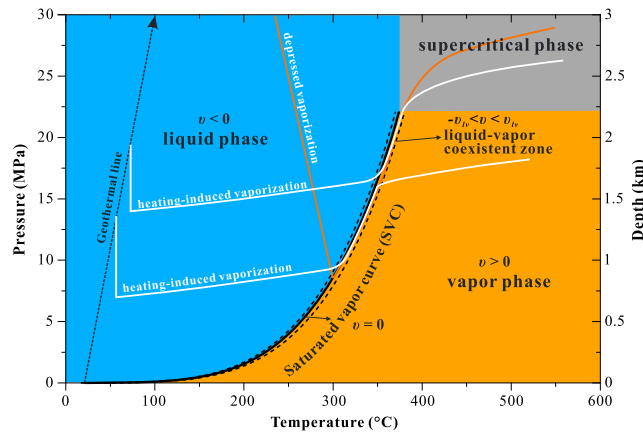
Figure 3. Pressure-temperature (PT) phase diagram of water and the inferred evolution curves of the PT state of pore water in the shear heated fault gouge zone, for two scenarios during the seismic slip of a natural earthquake. One is denoted in white lines, indicating the pore water vaporization induced by frictional heating at relatively shallow depths of the fault; the initial pressure drop is attributed to the dilatancy effect upon shear. The other is in a red line, indicating the pore water vaporization induced by depressurization which occurs at relatively greater depths. The black solid curve is the saturated vapor curve of water (SVC, also known as the coexistent curve or liquid-vapor transition curve). The space between the two dashed lines (as specified by $-v_{lv} < v < v_{lv}$) represents a two-phase coexistent zone (note that the width of this zone is exaggerated for plotting clarity). A state variable, v, is introduced to define the relation of a local PT state with respect to SVC, with its sign indicating the potential for vaporization/condensation and its absolute value indicating the vaporization/condensation rate.
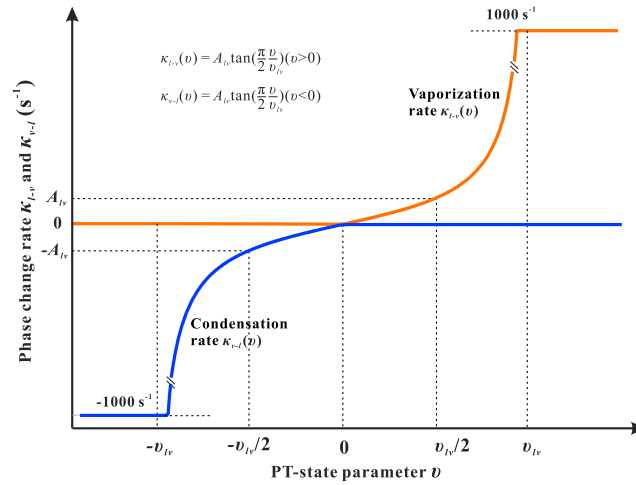
where $f_i(\xi)$ is a kinetic function determined by the rate-controlling mechanism of reaction (i). A temperature-dependent reaction rate is adopted following an Arrhenius law, $\kappa_i(T) = A_i\exp(-E_i/RT)$, where A_i is the rate constant (s^{-1}), E_i is the activation energy (K J mol^{-1}), and R is gas constant (8.31 J K^{-1} mol^{-1}). The effects of pressure and fluid chemistry on reaction kinetics are neglected because the relevant parameters are unavailable at present.

2.4. Phase Transition of Pore Water

Like a chemical reaction, the kinetics for a phase transition can be written as the summation of the forward and reverse "reaction" rates:

$$\frac{\partial S_v}{\partial t} = f_{l-v}\kappa_{l-v} + f_{v-l}\kappa_{v-l}, \qquad (10)$$

where κ_{l-v} and κ_{v-l} are the phase transition rates for the vaporization and condensation processes, respectively; f_{l-v} and f_{v-l} are the corresponding kinetic functions. For simplicity, we use the first-order functions, that is, $f_{l-v} = S_l$

and $f_{v-l} = S_v$. The kinetics of a phase transition, i.e., κ_{l-v} and κ_{v-l}, depends on heat flux, interfacial area, vapor pressure, and fluid chemistry and therefore cannot be readily expressed with some sort of equation like the Arrhenius law. An alternative approach to specifying the phase transition rate is required.

In thermodynamic equilibrium, when a phase transition occurs, the temperature should always be at the boiling temperature. Considering the intense heating inherent in natural earthquakes, thermodynamic equilibrium of pore water can be assumed, which means that when the temperature is above the boiling temperature, water cannot remain in the liquid state. As such, the kinetics of a phase transition is controlled by the Clapeyron relation, which characterizes a discontinuous phase transition between two phases of a single constituent. By definition, it is expressed as $\Gamma = \frac{\Delta h_{lv}}{T_{SVC}\Delta V_{lv}}$, where T_{SVC} is the boiling temperature (K), Δh_{lv} and ΔV_{lv} are the latent heat (J kg^{-1}) and the specific volume change (m^3 kg^{-1}) associated with the transition. Explicitly, the Clapeyron relation specifies the slope of the tangents to the saturated vapor curve in the PT phase diagram (Figure 3), that is,

$$\Gamma \equiv \frac{dp_{SVC}}{dT_{SVC}}. \qquad (11)$$

The saturated vapor curve (SVC, also known as the coexistence curve or liquid-vapor transition curve) can be represented by function F_{SVC}, expressed as follows:

$$p_{SVC} = F_{SVC}(T_{SVC}), \qquad (12)$$

where p_{SVC} is the saturated vapor pressure corresponding to a given T_{SVC}.

We let the phase transition rate depend on the local PT state with respect to the SVC. To implement this, we introduce a state parameter v, defined to be a function of pressure and temperature: $v = \frac{F_{SVC}(T)-p}{F_{SVC}(T)}$. In the phase diagram, a positive v value falls in the vapor regime, suggesting a potential for vaporization; a negative value falls in the liquid regime, suggesting a potential for condensation (see Figure 3). The absolute v value can be interpreted as the "distance" of a local PT state from the SVC, and a larger v value

Figure 4. Kinetics of the phase transition of pore water, as given by the annotated tangent functions (see also equations (13a) and (13b)). The red and blue lines are the phase transition rates for the vaporization ($\kappa_{l\text{-}v}(v)$) and condensation ($\kappa_{v\text{-}l}(v)$) processes, respectively. A threshold rate of 1000 s^{-1} is set to avoid the periodicity of a tangent function for large v values. Note that other types of function can also be used and would not change the modeling results. See details about the kinetic functions in the main text and Appendix C.

corresponds to a higher transition rate. To capture this feature, the "phase transition rate functions" are constructed in the tangent form

$$\kappa_{l-v}(v) = A_{lv} \tan\left(\frac{\pi}{2}\frac{v}{v_{lv}}\right)(v > 0)$$

(13a)

and

$$\kappa_{v-l}(v) = A_{lv} \tan\left(\frac{\pi}{2}\frac{v}{v_{lv}}\right)(v < 0)$$

(13b)

for the vaporization and condensation processes, respectively. Here v_{lv} is defined as a dimensionless (positive) constant and A_{lv} (in a unit of s^{-1}) is a reference transition rate when v equals $v_{lv}/2$. Figure 4 illustrates how the phase transition rates ($\kappa_{v\text{-}l}$ and $\kappa_{l\text{-}v}$) vary with the value of v. For example, in the case of positive v for a potential vaporiza-

tion process ($\kappa_{l\text{-}v} > 0$ and $\kappa_{v\text{-}l} = 0$), the vaporization rate $\kappa_{l\text{-}v}$ increases with increasing v value. Owing to the feature of a tangent function (equations (13a) and (13b)), $\kappa_{l\text{-}v}$ would increase to infinity as v approaches v_{lv}. The direct consequence is that accelerating vaporization will buffer the temperature rise and promote fluid pressurization, through the terms Q_{lv} and Ω_{lv}, respectively. Both effects would prevent the v value from increasing further ($v < v_{lv}$). As such, the parameter v_{lv} actually defines the width of the zone in which liquid and vapor phases can coexist, that is, $-v_{lv} < v < v_{lv}$ (as exaggerated in Figure 3 for plotting clarity), and the phase transition will be limited to occur within this zone.

In principle, to fully inhibit oversaturation (superheated liquid water or subcooled vapor water), the width of the coexistent zone ($2v_{lv}$) should be infinitesimally small. In practice, using a too small v_{lv} value requires very small time steps to avoid unstable behavior. This limits the convergence rate and raises enormous computational difficulties. In our modeling, we set v_{lv} to be 0.02 and A_{lv} to be 4 s^{-1}. A threshold rate of 1000 s^{-1} is set to avoid the periodicity of a tangent function for large v values (i.e., $|v| > v_{lv}$, Figure 4). Our verification tests show that the use of these values can sufficiently capture the features of the phase transition in a natural faulting process (see details in Appendix C).

2.5. The Final Equation Assembly

The final equation assembly consists of the heat equation (1), the mass balance equation (5), the reaction equation (9), and the equation for the phase transition (10). Following all the above considerations, we obtain the final system of equations:

$$S_s\frac{\partial p}{\partial t} = \frac{\partial}{\partial x}\left(\frac{k}{\eta_f}\frac{\partial p}{\partial x}\right) + \Omega_T + \Omega_{ch} + \Omega_{lv} - \frac{d\varphi_d}{dt}.$$

$$\rho_b c_b\frac{\partial T}{\partial t} = \frac{\partial}{\partial x}\left(K_b\frac{\partial T}{\partial x}\right) + Q_{fr} + Q_{ch} + Q_{lv}$$

$$\frac{\partial \xi_i}{\partial t} = f_i(\xi_i)\kappa_i(T)$$

$$\frac{\partial S_v}{\partial t} = f_{l-v}\kappa_{l-v} + f_{v-l}\kappa_{v-l}$$

(14)

In the absence of any phase transition, we have $\Omega_{lv} = Q_{lv} = S_v = 0$. This reduces equation set (14) into

$$S_s \frac{\partial p}{\partial t} = \frac{\partial}{\partial x}\left(\frac{k}{\eta_f}\frac{\partial p}{\partial x}\right) + \Omega_T + \Omega_{ch} - \frac{d\varphi_d}{dt}.$$

$$\rho_b c_b \frac{\partial T}{\partial t} = \frac{\partial}{\partial x}\left(K_b \frac{\partial T}{\partial x}\right) + Q_{fr} + Q_{ch} \tag{15}$$

$$\frac{\partial \xi_i}{\partial t} = f_i(\xi_i)\kappa_i(T)$$

This reduced system of equations is consistent with that previously proposed for TCP [*Sulem and Famin*, 2009; *Brantut et al.*, 2010; *Chen et al.*, 2013]. However, we want to emphasize that the differences between equation sets (14) and (15) are much more than just the phase transition terms, namely, Q_{lv} and Ω_{lv}. We wish to mention two main issues that are related to the occurrence of a phase transition.

The first issue concerns the fluid properties. An important consideration in the modeling of heat and fluid flow processes with phase transition is the choice of the primary variables that define the thermodynamic state of the system. When a new phase appears or disappears, Gibbs' phase rule states that the number of thermodynamic degrees of freedom will change. In a single-component flow process, the thermodynamic state variables for describing single-phase conditions (subcooled liquid water or superheated vapor water) are temperature and pressure. However, in two-phase conditions pressure and temperature are not independent but are related to one another by the saturated vapor (Clapeyron) relation. In our modeling, a "variable-switching" method has been adopted to deal with this problem: we use variables (pressure and temperature) for the single-phase condition and "switch" variables (to temperature and vapor saturation) when a transition to two-phase conditions occurs. We preserve temperature rather than pressure because in our modeled cases temperature tends to evolve more slowly than pressure. In "two-phase" conditions, all the fluid properties, i.e., density (ρ), specific heat (c), thermal conductivity (K), compressibility (β), thermal expansivity (α), dynamic and kinematic viscosities (η and ν), and relative permeability, are expressed as averaging functions of the vapor and liquid saturation (S_v and S_l), and the forms of the functions differ from property to property, depending on the thermodynamics of the two-phase flow system (Table 1). Detailed derivations for the mixture properties are given in Appendices A and B.

The other issue concerns the method for modeling a phase transition which we propose here. In this study, the kinetics of the phase transition ($\partial S_v / \partial t$) are forwardly modeled using the transition rate functions that are constructed in a tangent form (equations (13a) and (13b)). The phase transition criteria outlined in section 2.4 are very similar to the "finite window" method proposed by *Pruess* [2011] to deal with the phase transition between liquid and gaseous CO_2 under reservoir conditions. By introducing the concept of a coexistent zone for a phase transition, instead of applying some sort of "hair trigger" criterion, we achieve a more robust and efficient behavior in our simulations. Alternatively, transition rate functions of an exponential form can also be incorporated in the model (equations (C2a) and (C2b)) and essentially the same results are obtained. In addition, to further validate the method that we propose, we developed another system of equations to model a phase transition (C9a) and (C9b)); see derivations in Appendix C. These equations, directly constrained by the Clapeyron relation, do not even necessarily entail an explicit kinetic function. Yet the modeling results are in conformity with those obtained using the equation set (14).

3. Properties and Model Settings

3.1. Constitutive Relationships

Closure of the set of governing equations obtained above requires expressions for the properties of the mixtures. Specifically, when vaporization occurs, the pore fluid involves two phases, and the bulk sample becomes a solid-liquid-vapor multiphase system. The constitutive relationships between a mixture and its components are addressed in detail in Appendix B.

As summarized in Table 1, some fluid properties can be expressed as the arithmetic averages of the liquid and vapor phases, that is, $X_f = X_l S_l + X_v S_v$, where X indicates a given parameter (i.e., ρ, K, β, and α) and the subscripts l, v, and f represent the liquid phase, the vapor phase, and the mixture, respectively.

Specific heat of the pore fluid is given as $c_f = (\rho_l c_l S_l + \rho_v c_v S_v)/\rho_f$. Dynamic viscosity is determined by $\eta_f = \rho_f/(k_{rl}/v_l + k_{rv}/v_v)$, where k_{rl} and k_{rv} are the relative permeability for the liquid and vapor phases, respectively, and v_l and v_v are the corresponding kinematic viscosities, which are chosen as linear functions of the liquid or vapor saturation, that is $k_{rl} = S_l$ and $k_{rv} = S_v$ [*Shi and Wang*, 2011]. As pore water enters supercritical conditions, the phase of the pore water will be assigned as "liquid" when $S_v = 0$ and as "gas" when $S_v = 1$, depending on which side the fluid evolves toward relative to the SVC (Figure 3). We set $S_v = 1$ if the PT state evolves toward the higher-temperature side and $S_v = 0$ for the lower temperature side, which will allow the occurrence of further vaporization/condensation (if possible). The fluid properties in the supercritical regime are set as $X_f = X_l = X_v$, such that the above relations for liquid and vapor mixture are still valid. Density, thermal conductivity, and specific heat capacity of the bulk sample (ρ_b, K_b, and c_b) are functions of the gouge porosity, that is, $\rho_b = \rho_f \varphi + \rho_s(1-\varphi)$, $K_b = K_f \varphi + K_s(1-\varphi)$, and $c_b = [\rho_f c_f \varphi + \rho_s c_s(1-\varphi)]/\rho_b$, respectively, where the subscript "s" is reserved for the solids and "b" for the bulk sample.

It is noteworthy that for some properties, more elaborate functions or more sophisticated corrections are available in the literature. For instance, the thermal conductivity for a multiphase system can be expressed as a power law of the components, and the relative permeabilities are usually taken as cubic functions of individual components [e.g., *Shi and Wang*, 2011]. However, these details will make the model unnecessarily complex, and we chose to keep it as simple as possible by using approximate functions.

3.2. Fluid Properties Involving a Phase Transition

During seismic slip, PT conditions can vary over a wide range and the fluid properties, even for a single phase, can correspondingly undergo large changes [e.g., *Tanikawa et al.*, 2009; *Brantut et al.*, 2010; *Chen et al.*, 2013]. For instance, the viscosity of water can vary by 1 order of magnitude and compressibility by more than 2 orders of magnitude [*Chen et al.*, 2013] (see also *Sulem and Famin* [2009] for CO_2 fluid). These studies have shown that this variation of fluid properties during faulting plays a crucial role that can influence the slip process. In this study, as phase changes, the fluid properties may experience even larger variations due to the discontinuity along the phase transition line (Figure 2 and see more examples in *Chen et al.* [2013]).

To model the in situ conditions realistically, PT state-dependent fluid properties, i.e., density (ρ), specific heat (c), thermal conductivity (K), compressibility (β), thermal expansivity (α), and dynamic and kinematic viscosities (η and v), are introduced. These properties are interpolated from the database of the thermophysical properties of water (National Institute of Standards and Technology (NIST), available at http://webbook.nist.gov/chemistry/fluid/), including the liquid, vapor, and supercritical phases. Note that along the SVC, there exist two sets of water properties, for liquid and vapor phases, respectively (Figure 2). For a single-component flow process, the properties depend on the local temperature and pore pressure. To account for this, we employ a two-dimensional interpolation criterion, which involves a (bi) linear interior interpolation scheme for both temperature and pressure. In two-phase conditions, the interpolation is combined with the vapor saturation S_v. In other words, a fluid property, X_f, can be generally expressed as a function of temperature, pressure and vapor saturation: $X_f = X_f (T, p, S_v)$. Specifically,

i) when $S_v = 0$, pore water is in the liquid state so that X_f is interpolated from the liquid database, that is, $X_f = X_l (T, p)$;
ii) when $S_v = 1$, pore water is in the vapor state and X_f is interpolated from the gaseous database, that is, $X_f = X_v (T, p)$;
iii) when pore water enters the supercritical state, the phase can be arbitrarily assigned as liquid when $S_v = 0$, and as gas when $S_v = 1$, which does not affect the X_f value;
iv) when liquid and vapor phases are coexistent ($0 < S_v < 1$), the general function for X_f can be expressed as a sum of the single phases with some averaging algorithm (see section 3.1). Take ρ_f, K_f, β_f, and α_f, for instance, which can be written as the arithmetic average: $X_f = X_f (T, p, S_v) = S_l X_l (T, p) + S_v X_v (T, p)$. Following the Clapeyron relation, temperature and pressure are interdependent during a phase transition process, such that the above function can be simplified as $X_f = S_l X_l (T) + S_v X_v (T)$. Therefore, when a phase transition occurs, the two-dimensional interpolation criterion for fluid properties will reduce to one dimension.
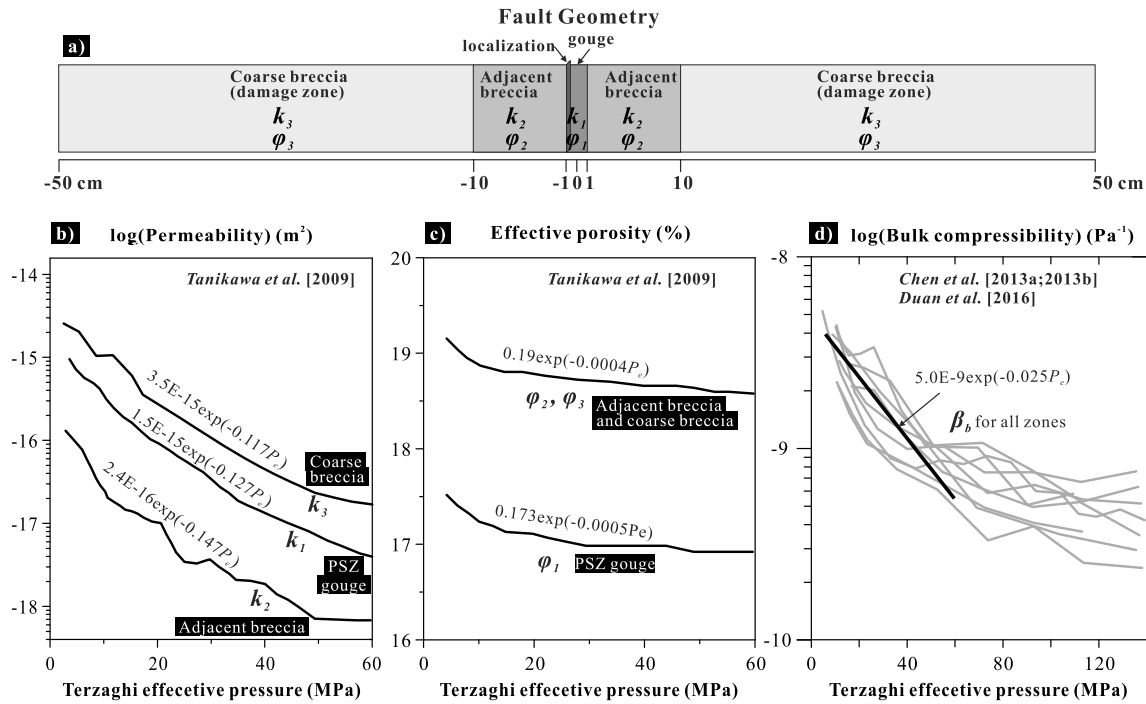
Figure 5. (a) The geometry of a representative fault zone modeled in this study, consisting of a central PSZ gouge zone, the adjacent fault breccia zones, and the outside damage zones (usually coarse fault breccias). The coseismic slip can be either uniformly distributed or localized at one margin of the gouge layer (2 cm thick). (b–d) Terzaghi effective pressure-dependent fluid transport properties assigned to the individual zones, including permeability Figure 5b, porosity Figure 5c, and bulk compressibility Figure 5d. The permeability and porosity data are results from measurements on material from the principal slip zone associated with the 1999 Chi-Chi earthquake that occurred on the Chelungpu fault [*Tanikawa et al.*, 2009]. The bulk compressibilities are the results of measurements on fault rocks from the Wenchuan earthquake fault [*Chen et al.*, 2013, 2016; *Duan et al.*, 2016], and the fitting only applies for the low-pressure range of data.

As addressed in section 2.5, in the model implementation, a variable-switching method has been adopted to deal with fluid properties: we use variables (T and p) for the single-phase condition and switch to variables (T and S_v) as a phase transition occurs. Finally, the latent heat of the phase transition (ΔH_{lv}) is determined as the difference of enthalpies between liquid and vapor water along the SVC (Figure 2d).

3.3. Fault Structure and Properties

In this section, we discuss all the fault-related parameters used in this study. In accordance with the typical fault core structure of a seismogenic fault zone, we construct a fault geometry of 1 m wide, consisting of a central gouge layer (2 cm thick), an adjacent breccia zones (10 cm for each side), and outside damage zones (coarse breccia zones) (Figure 5a). There are no variations in physical properties parallel to the fault. Frictional, fluid transport properties and mineralogical composition of the fault rocks are key parameters controlling the fault slip behavior. Shear-induced dilatancy, the width of the principal slip zone, and the depth of faulting are also important in determining whether a phase transition can occur or not. In what follows, we describe these key properties in more detail.

3.3.1. Frictional Properties

The dynamic friction coefficient (μ_d) of a fault gouge under wet conditions but without the effect of fluid pressurization is poorly constrained. In this study, except when stated otherwise, we use a constant μ_d of 0.6, a value chosen to agree with the frictional strength at low strain rates [e.g., *Rice*, 2006]. We investigate the effects of friction coefficient by either using a lower value (0.3) or letting it evolve with displacement (L). For the latter case, following previous HVF experiments [*Mizoguchi et al.*, 2007a], we use the equation $\mu_d = \mu_{ss} + (\mu_p - \mu_{ss}) \exp[\ln(0.05)L/d_c]$, where μ_p is peak friction (0.7), μ_{ss} is the steady state friction (0.3), and d_c is the slip-weakening distance (1 m), over which the stress reduces to 5% of the initial value.

3.3.2. Sliding Velocity

Earthquake slip rates can be as high as meters per second. In this study, except otherwise stated, a constant slip velocity of 0.5 m/s is used. To investigate its effect, we vary the (constant) slip rates

from 0.25 to 1 m/s. To simulate more realistic slip velocity history, we also use varying slip rate as done by *Sone and Shimamoto* [2009]. With a constant acceleration and deceleration rate (1 m/s^2), the slip velocity increases linearly from zero to 1 m/s in 1 s and then decreases, generating a total displacement of 1 m.

3.3.3. Transport Properties

Permeability and effective porosity of the principal slip zone (PSZ) gouge and the fault breccia zones are set as functions of Terzaghi effective pressure, $P_e = P_c - p$, where P_c is the confining pressure and in the present study, is equal to the normal stress σ_n acting on the fault plane (Figure 1). We use the experimental results of the fault rocks retrieved from the borehole of the Chelungpu fault that hosted the 1999 Chi-Chi earthquake, Taiwan [*Tanikawa et al.*, 2009]. An exponential law is used to fit the data according to $X = X_0 \exp(-\varepsilon P_e)$, where X_0 gives the permeability or porosity value at zero P_e and ε is the sensitivity to changes in pressure (Figures 5b and 5c). For permeability of the PSZ gouge, due to the strong hysteresis effect of pressure, only the data from the pressurization path are used to evaluate the initial values at the depth (or P_e) investigated, and the slope of the depressurization curve (with a ε value of -0.04) is used to calculate the permeability evolution due to pore fluid pressurization during faulting. For porosity, since its value changes little with decreasing pressure, the depressurization curve is not used to calculate its evolution.

Specific storage of a fault rock can be calculated as $S_s = \beta_b + \varphi\beta_f - (1 + \varphi)\beta_s$ [*Brace et al.*, 1968], where β_b is compressibility of the bulk sample, β_s is compressibility of the solid which is assumed to be constant (1.2×10^{-11} Pa^{-1}). *Tanikawa et al.* [2009] did report the specific storage data for the Chelungpu fault, but they used a constant fluid compressibility β_f in their calculation. In our model, β_f, as addressed above, is a function of temperature and pressure (or of temperature and vapor saturation). For bulk compressibility β_b, we use a fitting equation as a function of effective pressure based on data from nine natural fault rocks (refer to *Chen et al.* [2013, 2016], *Duan et al* [2016], plus two unpublished data sets, Figure 5d). Therefore, in our model, specific storage actually depends on effective pressure, temperature, pore pressure, and vapor saturation. Finally, we stress that fluid transport properties are usually measured under a hydrostatic loading condition which does not correspond to the in situ stress conditions during active faulting (nonhydrostatic loading and with shear-induced dilatation). In our modeling, we investigate this effect by varying the permeability and porosity of the gouge.

3.3.4. Shear-Induced Dilatancy

Assuming that seismic slip causes a 2% increase in the porosity ($\Delta\varphi_d$) and that the fault gouge has a specific storage (S_s) of 2×10^{-9} Pa^{-1} at 1–2 km depth (cf. Figure 5d), the pore pressure drop induced, as given by $\Delta\varphi_d/S_s$, is 10 MPa. This simple calculation implies that even at shallow crustal levels, shear-induced dilatancy can cause relatively large depressurization effects. In our modeling of a reference case which is at 1 km depth, it is assumed that dilatancy corresponds to a 5 MPa pressure drop. In the modeling, this is implemented by setting a lower value for the initial pore pressure within the principal slip zone (p_{PSZ}). To further investigate the dilatant effect, we also vary p_{PSZ} from p_a to 0.25 p_a, where p_a is the ambient pore pressure. Note that the shear-induced dilatancy is accompanied by a sudden increase in porosity, which is not considered in our model. Nonetheless, since all the dilatancy essentially occurs in the earliest stage of slip, this effect can still be simulated by varying the initial porosity of the gouge.

3.3.5. Slip Band Thickness

The least well-defined parameter is the width of the shear band (w), accommodating slip. Field observations and experimental studies show that the slip of a seismic event might be highly localized [e.g., *Chester and Chester*, 1998]. Here we assume that all the displacement is accommodated within the gouge layer which has a thickness of W, but the slip distribution over the layer can be either even ($w = W$) or localized ($w < W$, Figure 5a). In the latter case, we let the slip be localized at one margin of the gouge zone, with the width of the zone, w, varying from 5 mm to 15 mm.

3.3.6. Depth

A reference case is set at a depth of 1 km, and we also run models at varying depths from 0.5 to 3 km. Assuming hydrostatic conditions ($p_a = 0.4P_c$) and imposing the dilatant effect as above, the p_{PSZ} values at these depths are below the critical pressure so that the pore water is initially in a liquid state. We stress that at greater depths where the pore water is supercritical, as proposed by *Weatherley and Henley* [2013], vaporization can still occur but in a different scenario (Figure 3). However, this is beyond the scope of this study.

Table 2. Parameters Used in the Modeling[a]

Parameters	Symbol	Values[b]	Units	Reference (Note)
		Fault Zone Configuration		
Slip velocity	V	0.5 [0.25–1]	ms^{-1}	This study
Time span of slip	t_s	2	s	This study
Slip band thickness	w	20 [5–20]	mm	This study
Depth	z	1.0 [0.5–3]	km	This study
Thermal gradient	dT/dz	25	$°C\ km^{-1}$	This study
Hydrostatic/lithostatic pressure coefficient	λ	0.4		This study
Friction coefficient	μ_d	0.6 [0.3, 0.7 → 0.3]		This study and *Mizoguchi et al.* [2007a]
		Solid and Fluid Properties		
Specific heat of solid grains	c_s	650	$J\ kg^{-1}\ K^{-1}$	*Hemingway* [1987]
Thermal conductivity of solid grains	K_s	3	$Wm^{-1}\ K^{-1}$	*Tanaka et al.* [2006]
Density of solid grains	ρ_s	2.7×10^3	$kg\ m^{-3}$	*Chen et al.* [2013]
Thermal expansivity of solid grains	α_s	2.2×10^{-5}	K^{-1}	*Bayer* [1973]
Compressibility of solid grains	β_s	1.2×10^{-11}	Pa^{-1}	*Birch* [1966]
Liquid water properties ($X = c, K, \rho, v, \eta, \alpha$ and β)	X_l	PT dependent		NIST
Vapor water properties ($X = c, K, \rho, v, \eta, \alpha$ and β)	X_v	PT dependent		NIST
		Reaction Parameters		
Reactant concentration (smectite)	ω_{sm}	0 [20%]	wt %	with one interlayer of water
Molar enthalpy change of smectite dehydration	ΔH_{sm}	−43000	$J\ mol^{-1}$	*Chen et al.* [2013]
Reaction rate constant of smectite dehydration	A_{sm}	553	s^{-1}	*Noyan et al.* [2008]
Activation energy of smectite dehydration	E_{sm}	32200	$J\ mol^{-1}$	*Noyan et al.* [2008]
Mole number of water in smectite	χ_{sm}	2.0		*Chen et al.* [2013]
Volume loss of solids by smectite dehydration	ΔV_{sm}	0.194		*Huang et al.* [1994]
Specific expelled water by smectite dehydration	Π_{sm}	8.2%		*Chen et al.* [2013]
		Transport Properties		
Gouge zone permeability	k	k_1 [$10k_1$–$0.001k_1$]	m^2	*Tanikawa et al.* [2009] and Figure 5
Gouge zone porosity	φ	17.3% [4%–21%]		*Tanikawa et al.* [2009] and Figure 5
Breccia zone permeability	k	$k_2; k_3$	m^2	*Tanikawa et al.* [2009] and Figure 5
Breccia zone porosity	φ	$\varphi_2; \varphi_3$		*Tanikawa et al.* [2009] and Figure 5
Bulk compressibility	β_b	$5 \times 10^{-9}\exp(-0.025P_e)$	Pa^{-1}	*Chen et al.* [2013, 2016] and Figure 5
		Shear-Induced Dilatancy		
Dilation-induced porosity change	$\Delta\varphi_d$	~1%		This study
Initial pore pressure in the shear band	p_{PSZ}	0.5 [0.25–1]p_a	MPa	This study
		Phase Change Parameters		
Vaporization/condensation rate constant	A_{lv}	4 [1–8]	s^{-1}	This study
Threshold state value for vaporization	v_{lv}	0.02 [0.005–0.05]		This study
Enthalpy change associated vaporization	ΔH_{lv}	PT dependent	$J\ mol^{-1}$	NIST

[a]The thermophysical properties of liquid and vapor phases of water are set to be dependent on pressure and temperature (PT dependent); their values are from NIST (download from the website http://webbook.Nist.Gov/chemistry/fluid/).

[b]Values before the brackets are used in the reference case (section 4.1), and values in brackets are used for parametric analyses (sections 4.2–4.9 and Appendix C).

3.3.7. Chemical Reaction(s)

Chemical reactions have similar effects as vaporization. For comparison purposes, in one model, the fault gouge is assumed to contain 20 wt % smectite. We assumed that the smectite carries one interlayer of H_2O in the unit lattice cell, and losing it can cause a solid volume reduction of 19.4% [*Chen et al.*, 2013; *Schleicher et al.*, 2015]. A first-order kinetic function is adopted such that $f(\xi) = 1 - \xi$ [*Huang et al.*, 1994]. Detailed kinetic parameters for smectite dehydration as well as the other parameters used in the modeling are listed in Table 2.

3.4. Model Settings

The one-dimensional planar fault model shown in Figure 5 is represented by a mesh containing a total of 1280 elements, 128 of which occupy the gouge zone. We take zero-flux boundaries for the fluid and temperature fields. A uniform initial temperature is assigned on the basis of a geothermal gradient of 25°C/km. The initial pore pressure (p_a) is set to be hydrostatic, with a hydrostatic/lithostatic coefficient λ of 0.4 ($p_a = 0.4P_c$). Within the shear band, the value is lowered by a certain amount ($p_{PSZ} \le p_a$) according to the dilatant effect assumed.

The coupled partial differential equations describing energy balance, fluid mass transport, chemical reactions, and the fluid phase transition (equation set (14)) are solved using finite element software (COMSOL 3.5), solving simultaneously for all dependent variables including pore pressure (p), temperature (T), vapor saturation (S_v), and reactant concentrations (ξ). All these variables, together with the nonlinear parameters that are coupled to these variables (e.g., permeability, porosity, and different fluid properties), are sequentially iterated until the global error meets the relative and absolute tolerances in each time step. It is worthwhile to note that the mean pore pressure inside the slip zone ($\bar{p}$) is included in the iteration. As an "integration coupling variable", in each iteration step, it is calculated by integrating the pore pressure over the slip band and dividing it by the width of the slip band.

Our modeling addresses a time interval totaling 2.5 s, with the slip lasting for the first 2 s, producing a displacement of 1 m (with a constant slip velocity of 0.5 m/s, to simulate an earthquake magnitude of ~6.0). This excludes three cases in which we either use varying slip rate or varying friction coefficient or investigate the fault slip at 0.5 km depth. For the first case, slip times are adjusted correspondingly to produce a total displacement of 1 m, while for the latter two, we find that the frictional heat generated by 1 m displacement as in the other cases is not enough to cause vaporization or to reach steady state; therefore, we extend the slip period to 4 seconds to produce a displacement of 2 m. The time step is set to be 0.01 s before the occurrence of a phase transition (or a chemical reaction) and is then changed to 0.001 s.
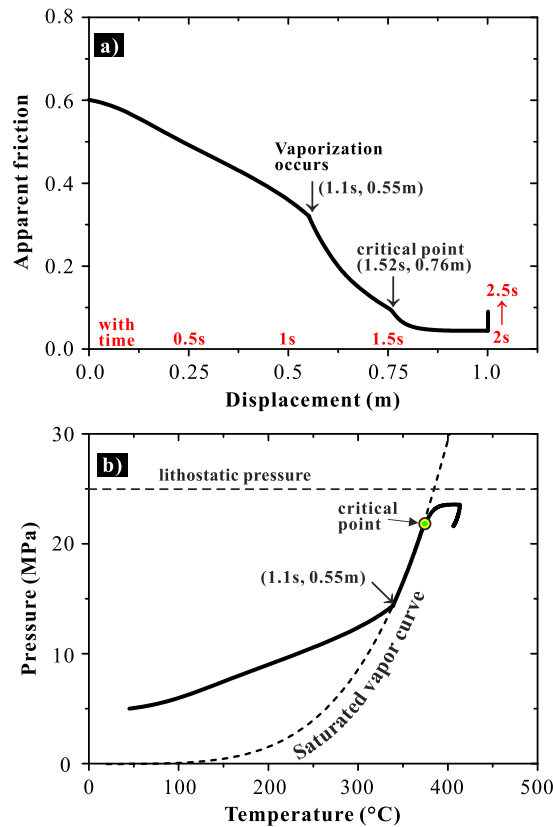
4. Modeling Results

Our models calculate the evolution of pore pressure (p), temperature (T), reactant concentration (ξ), and vapor saturation (S_v) as a function of time and distance from the slip surface. From these results, we can obtain the evolution of all the parameters that are coupled to these variables (e.g., fluid viscosity, gouge porosity, and effective pressure). In this study, we focus on the following parameters.

1. The slip-weakening effect can be evaluated by the evolution of *apparent friction coefficient* (μ_a), defined as the shear stress over the initial effective normal stress, i.e., $\mu_a = \tau/(\sigma_n - p_{PSZ})$.
2. The evolution of pressure and temperature state (*PT state*) is compared with the saturated vapor curve (SVC) in the phase diagram of water.
3. As addressed later, the occurrence of vaporization and the resultant slip weakening are related to the *frictional work* W_f (total mechanical work per unit fault area) done to the system, which can be calculated as the integral of shear stress over displacement (L), $W_f = \int \tau dL = (\sigma_n - p_{PSZ}) \int \mu_a dL$. We define W_{cr} to be the critical frictional work corresponding to the onset of vaporization.
4. Finally, the temperature and pore pressure evolution during seismic slip are attributed to the individual terms embodied in the governing equations. Specifically, the *fluid pressurization* is controlled by the interplay between thermal pressurization, fluid mass liberation from chemical reaction, vaporization, and fluid loss by drainage from the heated zone, while the *temperature rise* is attributed to frictional heating, thermal diffusion, and the heat sinks provided by the chemical reaction(s) and the phase transition.

In the following, we first present results from a reference case (section 4.1), in which the parameters are chosen to be representative of a natural fault zone (e.g., the Chelungpu fault). To consider the parametric effects addressed in section 3.2, comparative models are presented in sections 4.2–4.9. In each individual section, we vary one single parameter with respect to the reference case, with all other parameters remaining the same. In doing this, we neglect any potential interdependence between different parameters, such as that between porosity and permeability.

4.1. The Reference Case

First, we model a reference case (referred to as "*Ref*" hereafter). In this case, the coseismic slip is evenly distributed over the 20 mm thick gouge zone at 1 km depth and subjected to a confining pressure (P_c) of 25 MPa, an ambient pore pressure (p_a) of 10 MPa, and temperature (T_a) of 45°C, with a constant friction coefficient (μ_d) of 0.6, a constant shear velocity (V) of 0.5 m/s, and shear-induced dilatancy corresponding to a 5 MPa pressure drop in the shear band. Under these conditions, the fault gouge has an initial permeability, porosity, and specific storage of 1.2×10^{-16} m^2, 17.3%, and 6.1×10^{-9} Pa^{-1}, respectively. The modeling results are shown in Figures 6 and 7. Within the 2 s of slip, the apparent friction (μ_a)

Figure 6. Modeling results of the reference case ("*Ref*"). In the "*Ref*" case, the coseismic slip is evenly distributed over the 2 cm thick gouge zone and the fault is at 1 km depth, with a constant friction coefficient of 0.6, constant sliding velocity of 0.5 m/s, and shear-induced dilatancy corresponding to a 5 MPa pressure drop. Details of the modeling conditions for the "*Ref*" case are explained in the text and Table 2. (a) The evolution of apparent friction coefficient with displacement (and time). (b) The evolution of the PT state of the pore fluid at the center of the PSZ, with the saturated vapor curve and critical point of water being added for comparison. In Figure 6b, the extension cord of the saturated vapor curve beyond the critical point (see the dashed line in the supercritical state) is obtained from the density contour map (Figure 2a), from which the individual point is chosen at which the density has the highest gradient with respect to temperature (which can be specified as $(\partial^2 \rho/\partial T^2)_P = 0$).
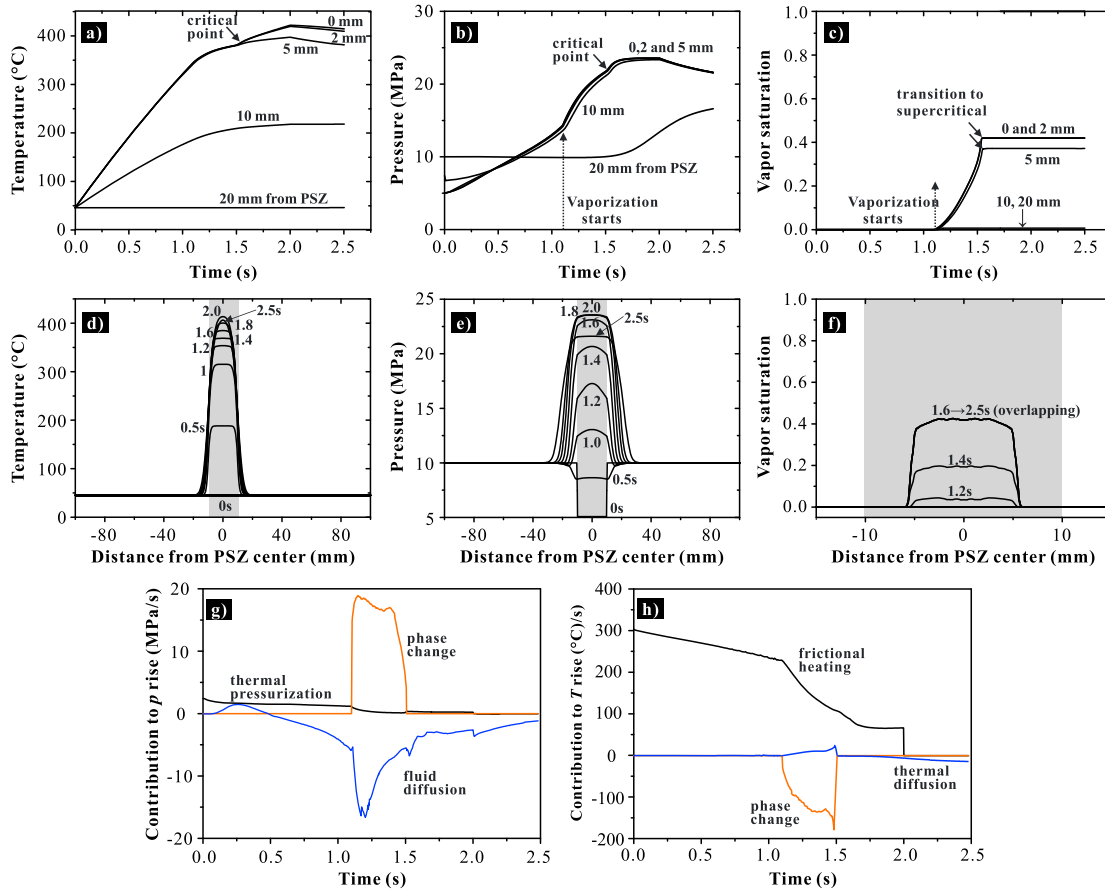
first drops from 0.6 to 0.35 in the first 1.1 s (or 0.55 m displacement), which is followed by a further sharp decrease to a final steady state value of ~0.05 (Figure 6a). The PT state evolution at the center of the PSZ shows a slight increase in the first 0.55 m displacement and then evolves tightly along the saturated vapor curve (SVC) of water until reaching the critical point (Figure 6b). As the slip continues, the PT state evolution deviates from the SVC and then shows more or less a pure rise in temperature. As the slip stops, both the temperature and pore pressure decrease. We remark in the first place that the transition to a sharp slip weakening coincides with the onset of water vaporization (at 1.1 s, cf. Figures 6a and 6b).

By the end of 1.0 m displacement, the maximum temperature reaches ~400°C at the center of the PSZ (Figure 7a). The maximum pore pressure of ~23 MPa is achieved at ~1.7 s, and afterward, the pore pressure remains nearly constant (Figure 7b). The vapor saturation curves show that the phase transition starts at 1.1 s at the PSZ center, and 40% of the pore water has vaporized before transforming into the supercritical state (Figure 7c). Snapshots of the temperature, pore pressure, and vapor saturation fields in time are presented in Figures 7d–7f, respectively. The shape of the pore pressure profiles versus distance from the PSZ center is wider than that for the temperature field, suggesting higher efficiency in fluid diffusion than heat transport. The phase transition is limited to the central 10 mm of the PSZ during the entire slip event (Figure 7f).

Our calculations further show that at the early stage of slip (<1.1 s), the pore pressure builds up mostly due to the thermal pressurization (TP) effect and after that vaporization begins to be dominant, with a fluid pressurization rate that is ~10 times the rate by TP (Figure 7g). This situation continues until the pore fluid becomes supercritical (>1.52 s). During this phase transition interval (1.1–1.52 s), the fluid diffusion by Darcy flow also becomes more important due to the pressurized pore fluid and the decrease in fluid viscosity. In terms of energy partitioning, thermal diffusion only takes up a negligible portion of the frictional work done by the seismic slip (Figure 7h). However, the phase transition behaves as a dominant heat sink upon its occurrence (Figure 7h). At the same time, fluid pressurization accelerates so that effective normal stress decreases, which in turn causes a decrease in the rate of frictional heat production (cf. Figures 7g and 7h).

Finally, it might be interesting to point out that the pore fluid at the central slip zone (within 5 mm away from the center) show a secondary rapid increase in pore pressure after reaching the supercritical state (1.52–1.7 s, Figure 7b), corresponding to a reinforced slip weakening (Figure 6a). Similar phenomena are also predicted in the following cases of modeling (Figures 8–14). Beyond the critical point, the buffering effect associated with the phase transition does not play a role, giving rise to a more rapid increase in temperature (Figure 7a) and

Figure 7. Detailed modeling results of the reference case ("*Ref*," as Figure 6). The evolution of (a) temperature, (b) pore pressure, and (c) vapor saturation with time at various distances (0, 2, 5, 10, and 20 mm) from the PSZ center. Snapshots of the fault-perpendicular distribution of (d) temperature, (e) pore pressure, and (f) vapor saturation. (g) Comparison of the pore pressure contributions from thermal pressurization, fluid diffusion and phase transition. (h) Comparison of the temperature rise caused by frictional heating, thermal diffusion and phase transition. The shaded areas in Figures 7d–7f denote the central gouge zone (20 mm in width). Note that in a typical simulation, when pore water enters supercritical conditions, the phase of the pore water will be arbitrarily assigned as liquid when $S_v = 0$ and as gas when $S_v = 1$. This will allow the occurrence of further vaporization/condensation process (if possible). In the simulation shown here, in order to know how much pore water has been vaporized during the slip (as given in Figures 7c and 7f, with a maximum of ~40%), we fix S_v when reaching the critical point. We note here that this setting does not affect other results (if S_v is not fixed, it will evolve to 1 in this case, since the pore water goes to the high-temperature side beyond the critical point, see Figure 6).

thus in TP rate (Figure 7g). At the same time, when the pore water evolves toward higher temperature in the supercritical regime, the fluid properties change rapidly (Figure D1), causing a decrease in the fluid dissipation rate (Figure 7g).

4.2. The Effect of Friction Coefficient

In the reference case, we used a constant value of 0.6 for friction coefficient. Here we vary the model by either using a lower friction coefficient (0.3) or allowing it to evolve with displacement (*L*). As shown in Figure 8a, for all the *cases* investigated, the PT state evolution curves show almost the same pattern, that is, once pore water starts to vaporize, the PT state evolves along the SVC until reaching the critical point. The progression along the SVC with the development of time and displacement, however, is very different: slip weakening is more rapid at higher constant friction ($\mu_d = 0.6$ versus 0.3, Figure 8b), and even more so in the case of *L*-dependent friction. We attribute the latter behavior to the combined effects of fluid pressurization and the declining friction coefficient (indicated by the dashed curve in Figure 8b). So the time or displacements required for vaporization to occur are diverse in different cases (Figure 8b), but when we evaluate the frictional work (W_f), a constant critical value W_{cr} of 5.2 M J/m^2 can be obtained (Figure 8c; see a theoretical analysis for the consistent frictional work in section 5.2).
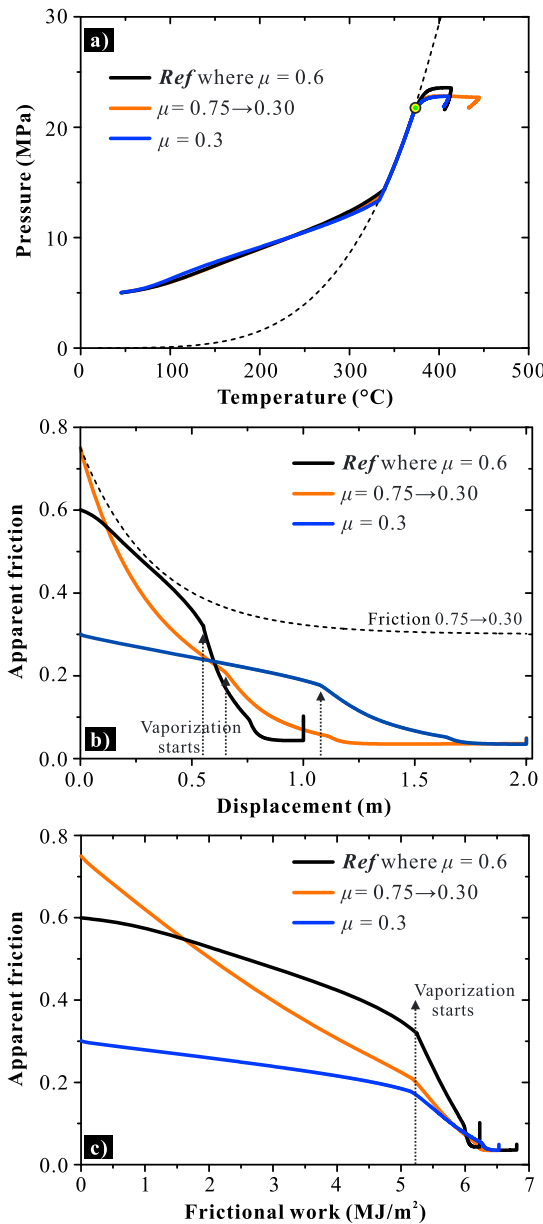
Figure 8. Modeling results of the cases with different settings for the dynamic friction coefficient. (a) The evolution of the PT state of pore water at the PSZ center. (b) The evolution of apparent friction with displacement. (c) The evolution of apparent friction with the total frictional work. The results from the "*Ref*" case are added for comparison.

4.3. The Effect of Sliding Velocity

To represent the variation of seismic slip rates, we tested models with different (constant) sliding velocities (0.25–1 m/s). In each case, the duration of coseismic slip was adjusted accordingly to generate a 1 m displacement. For all the velocity range investigated, the results of the PT state evolution do not show much difference, except that when the fault moves at higher slip rates, higher pore pressures and lower steady state friction coefficients are achieved by the end of slip (Figure 9a). We also used varying slip rates from zero to 1.0 m/s and back to zero in 2 s, which also generates 1 m displacement. The results are again similar to the reference case which has a constant slip rate of 0.5 m/s (Figure 9a), except that the restrengthening starts earlier in the case of varying velocity (when the slip rate decelerates to 0.3 m/s). The frictional work for the onset of vaporization is not sensitive to sliding velocity either, indicating the same W_{cr} value (5.2 M J/m^2) as the reference case (Figure 9b).

4.4. The Effect of Permeability

We investigated the effect of fluid diffusion efficiency by varying the permeability of the PSZ fault gouge by up to 4 orders of magnitude. Modeling results with variable gouge permeabilities do not differ much from the reference case, except that for lower permeabilities, higher pore pressures (or lower dynamic friction) can be achieved (Figure 10a). Some models even predict a superlithostatic, local pore pressure (i.e., when $k < 0.01 \, k_1$). Note that this overshoot only occurs in part of the thickness of the shear band, i.e., in the central zone. The average pore pressure ($\bar{p}$) does not exceed the normal stress acting on the fault plane, thus still preserving some

shear resistance (Figure 10b). Once overshoot occurs, the equation used for fluid flow cannot accurately describe the system any longer because of possible non-Darcy flow. The slip-weakening effects in all of these cases, as reflected by the evolution of apparent friction coefficients (Figure 10b), are similar. Apparently, they have the same W_{cr} value corresponding to the onset of vaporization (5.2 M J/m^2).
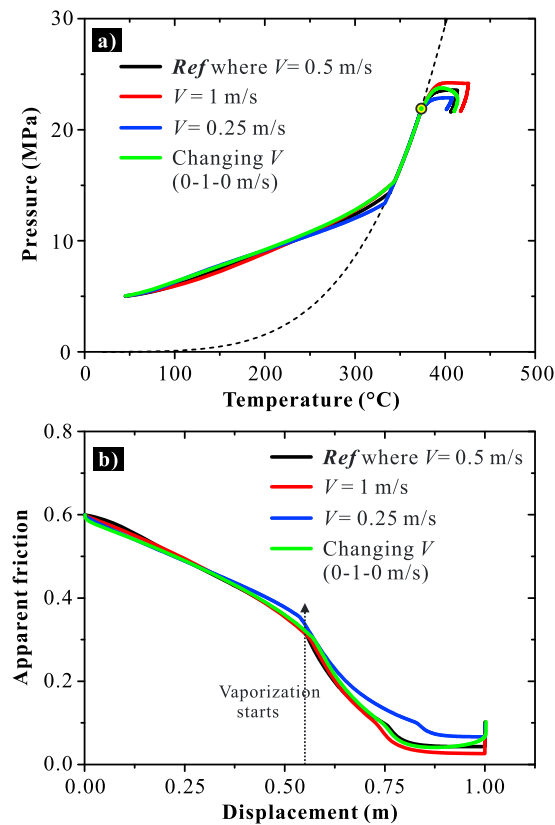
4.5. The Effect of Porosity

The porosity controls the amount of water available for vaporization in a unit volume of fault gouge. To compare with the reference case (Figure 5c), we use a P_e-dependent porosity function $\varphi = \varphi_0 \exp(\varepsilon P_e)$, in which the pressure sensitivity ε is set to be the same as the reference case (-0.0005) but φ_0 is varied from 4% to 21%. Modeling results for different gouge porosities are shown in Figure 11. When the porosity is higher,

Figure 9. Modeling results of the cases with different (constant or varying) slip rates. (a) The PT state evolution of pore fluid at the PSZ center. (b) The evolution of apparent friction with displacement. The results from the "*Ref*" case are added for comparison.

the evolution of the PT state of pore water exhibits a more rapid increase in pressure than in temperature during the early stage of the slip (before the onset of vaporization), and lower temperature is achieved by the end of the slip (Figure 11a). This can be explained by the increase in heat capacity of the gouge with increasing porosity since the liquid water has higher specific heat than the solids (see section 5.2 for quantitative analysis). The evolution of apparent friction coefficient with displacement shows the same trend for the early stage of slip, but vaporization occurs earlier in the less porous slip zones (Figure 11b). Correspondingly, less frictional work is required to reach the boiling temperature for vaporization (Figure 11c). The critical frictional work W_{cr} shows a clear linear relation with gouge porosity (Figure 11d).

4.6. The Effect of Shear-Induced Dilatancy

In the reference case, shear-induced dilatancy is taken into account by setting the initial pore pressure within the shear band (p_{PSZ}) lower than the ambient pore pressure (p_a). To investigate the role of quasi-instantaneous dilatancy in the phase transition and the associated slip-weakening effect, we run models with different p_{PSZ} values (0.25–1.0 p_a). As shown in Figure 12a, for all the p_{PSZ} values investigated, the PT state evolution curves show the same pattern, that is, the PT state evolves along the SVC upon reaching it. Stronger dilatancy corresponds to lower p_{PSZ} value and thus higher effective normal stress, giving rise to more rapid TP and slip weakening at the early stage of slip (prior to the sharp weakening corresponding to vaporization, Figure 12b). At the same time, more rapid frictional heating causes an earlier occurrence of the vaporization (Figure 12b). Again, if we plot the apparent friction against the total frictional work (W_f), the results for the different cases converge (Figure 12c). Vaporization and the resultant rapid weakening occur at roughly the same frictional work (W_{cr} value of 5.2 M J/m^2) for all the cases investigated.

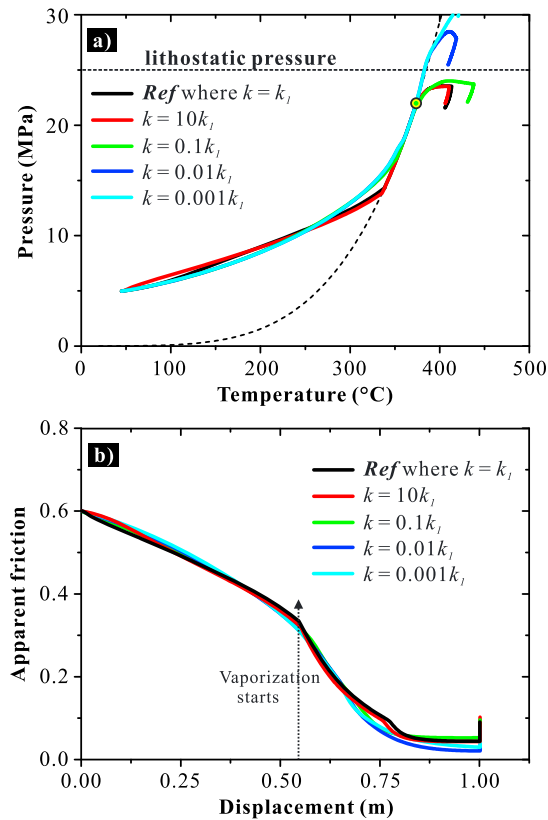### 4.7. The Effect of Slip Localization

Field observations and microscopic analyses on both natural and lab-sheared fault gouges suggest that coseismic slip might be localized [e.g., *Rice et al.*, 2014]. Slip localization is considered by letting slip occur at one margin of the gouge zone resembling the real fault structure. In this case, the mesh grid was refined to make sure that the active slip zone is occupied by more than 36 elements. As shown in Figure 13a, the PT state evolution curves show higher slopes with decreasing slip band thickness, implying that a localized slip can cause a faster rise in temperature than in pore pressure. The faster rise in temperature also leads to higher efficiency in TP, giving rise to faster slip weakening (Figure 13b). As a consequence, less frictional work (Figure 13c) is needed for a thinner slip zone to reach the boiling temperature for vaporization. The critical frictional work (W_{cr}) turns out to be linearly proportional to the shear band thickness (Figure 13d). It is important to point out that as the slip gets more localized, the apparent steady state friction increases (Figure 13b). Considering the structure of the fault zone modeled (Figure 5), we infer that this is due to the decrease in

Figure 10. Modeling results of the cases with variable permeabilities for the PSZ fault gouge. The permeability is varied by 4 orders of magnitude, from the order of 1×10^{-15} m^2 ($k = 10\,k_l$) to 1×10^{-19} m^2 ($k = 0.001\,k_l$). (a) The evolution of the PT state of pore fluid at the PSZ center. (b) The evolution of apparent friction with displacement. The results from the "*Ref*" case are added for comparison.

diffusion length with increasing degree of localization, which leads to a lower (steady state) pore pressure and thus higher effective normal stress [see also *Chen et al.*, 2013].

4.8. The Effect of Depth

We varied the depth of the model from 0.5 to 3.0 km with an interval of 0.5 km. Note that in the case of 0.5 km depth, we extended the slip period to 4 s in order to generate enough frictional heat to cause vaporization. At greater depth, the increased normal stress implies that more frictional heat can be generated, while the fault rocks are expected to be more impermeable [e.g., *Tanikawa et al.*, 2009]. With a given hydrostatic/lithostatic pressure coefficient ($\lambda = 0.4$), an increase in depth also elevates the average pore pressure. Both effects would render the phase transition difficult to occur.

Indeed, the PT state evolution curves at depths greater than 1.5 km do not reach the SVC in the phase diagram (Figure 14a). However, the pore pressure and temperature at these depths still rise fast, with the PT state appearing to evolve along the extension cord of the SVC. As a consequence, the evolution of apparent friction for all the depths investigated shows strong slip weakening, although, at depths greater than 1.5 km, the resultant sharp weakening is not visible due to the absence of vaporization (Figure 14b). When plotted against frictional work, the apparent friction shows similar weakening for all cases investigated (Figure 14c). One surprising result we find here is that the apparent steady state friction coefficients increase with increasing depth (Figure 14b). This is in contrast with the previous modeling of TP without incorporating phase transition [e.g., *Wibberley and Shimamoto*, 2005; *Chen et al.*, 2013; *Tanikawa et al.*, 2013]. In these previous models, TP gets more efficient at greater depth, leading to a lower steady state apparent friction coefficient.
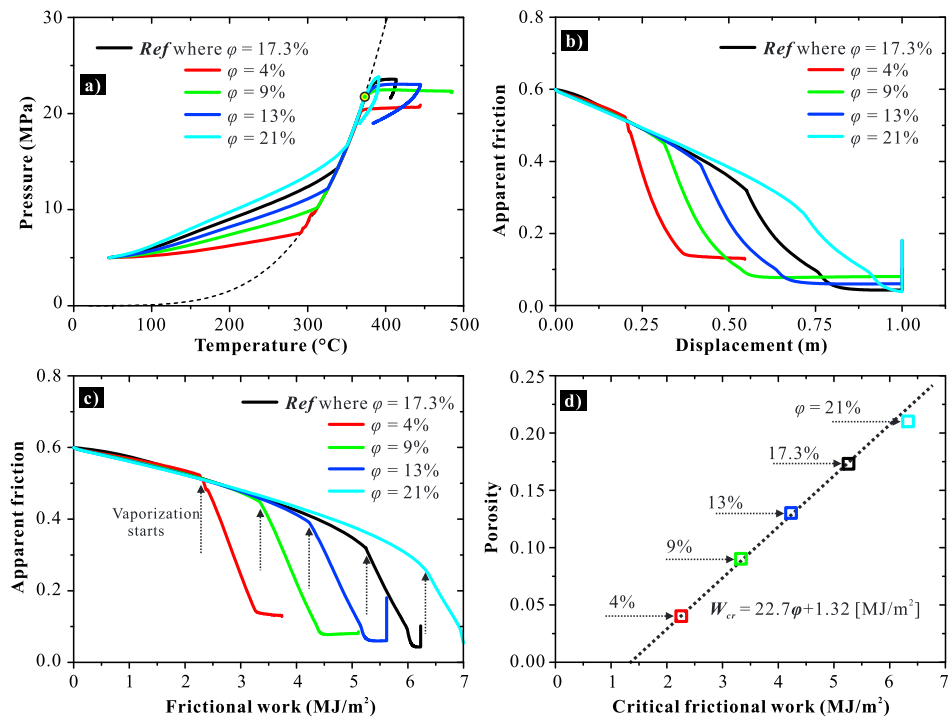
4.9. In the Presence of a Chemical Reaction

Similar to water vaporization, a dehydration reaction is endothermic and can enhance fluid pressurization [e.g., *Brantut et al.*, 2010]. We performed a last simulation for a fault gouge containing 20 wt % smectite. According to the kinetic parameters (Table 2) [*Huang et al.*, 1994], smectite starts to dehydrate at around 80°C. The modeling results show that the PT state evolution in the presence of smectite is almost the same as the reference case (except for lower temperature being achieved by the end of slip, Figure 15a), while a slightly larger displacement (or longer time) is needed for the onset of vaporization (Figure 15b). By the end of slip, 75% of the smectite contained in the gouge has lost the interlayer water (Figure 15b). In terms of fluid pressurization, the dehydration contributes much less than the phase transition, and TP is only important at the early stage of slip before either vaporization or dehydration becomes active (Figure 15c). In terms of energy partitioning, however, thermal pressurization plays a dominant role over the entire slip period, and the endothermic effects of vaporization and dehydration are comparable to one another (Figure 15d). Meanwhile, the occurrence of vaporization can cause a decrease in heat generation rate due to the remarkable pressurization effect (cf. Figures 15c and 15d).

Figure 11. Modeling results of the cases with variable porosities (φ) for the PSZ fault gouge. (a) The evolution of the PT state of pore fluid at the PSZ center. (b) The evolution of apparent friction with displacement. (c) The evolution of apparent friction with the total frictional work, in which critical frictional work W_{cr} for the onsets of vaporization (or sharp slip weakening) are indicated by the dashed line arrows. (d) A linear relation exists between W_{cr} and the PSZ porosity (φ). The results from the "*Ref*" case are added for comparison.

5. Discussion

5.1. Challenges of Modeling Coseismic Slip With Phase Transition

Numerical modeling of the heat transfer and fluid flow processes in the presence of two fluid phases in a deforming fault zone is intrinsically complicated and requires some simplifications. The main challenges lie in the strong, nonlinear coupling of the governing equations as well as the treatment of the phase transition.

First, this study employs a two-phase mixture model. The set of equations derived resembles the single-phase formulations for thermochemical pressurization [e.g., *Sulem and Famin*, 2009; *Chen et al.*, 2013] and reduces to them when the vapor saturation (S_v) becomes zero. Our mixture model is thus valid throughout the entire domain including both the single-phase and two-phase regimes (if present), which is a key advantage. Of course, to fully retain the characteristics of the two-phase fluid flow, complex algebraic relations are needed to describe the equivalent properties of the mixture (Table 1).

Second, in this study, by introducing the concept of a "coexistent zone" and constructing the artificial kinetic functions for the phase transition, which is done mathematically rigorously, we can simulate the vaporization and condensation processes without the loss of accuracy. The parameters (A_{lv} and v_{lv}) introduced in the kinetic functions have their physical meanings, as they are similar to the reaction rate constants for a chemical reaction. Interestingly, the modeling results, as addressed in Appendix C, turn out to be neither sensitive to the values of these parameters nor to the form of the functions adopted. Why is that? We attribute this to the conformity of a phase transition with the Clapeyron relation. In the presence of a phase transition, the two-phase coexistent region can be assumed to be isothermal, especially when the two phases are of a single constituent (H_2O in our case). For a uniform temperature field, the energy conservation equation will reduce to the mass conservation equation [*Wang and Beckermann*, 1993]. This is intuitive because without a thermal gradient, i.e., $\nabla \cdot (K_b \nabla T) = 0$, the energy transfer in the system is only attributed to the phase transition (provided that there is no chemical reaction involved). In other words, when a phase transition occurs, the local temperature and pressure at an arbitrary point of the gouge are
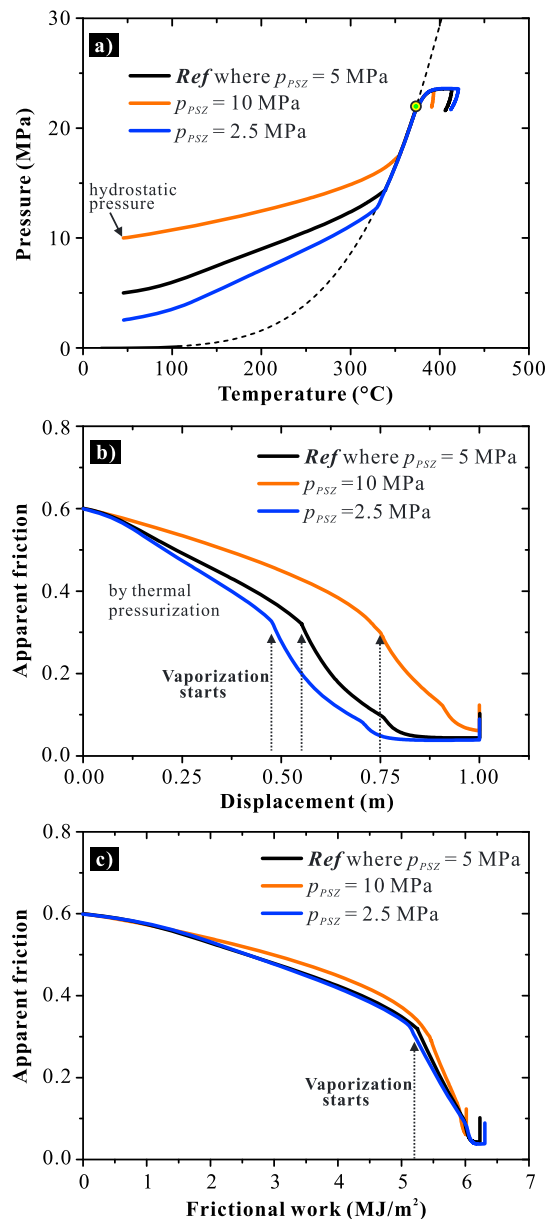
Figure 12. Modeling results of the cases with varying degrees of shear-induced dilatancy, which is simulated by setting different initial pore pressure in the active shear band (p_{PSZ}). (a) The evolution of the PT state of pore fluid at the PSZ center. (b) The evolution of apparent friction coefficient with displacement, in which the transition to a sharp weakening corresponds to the onset of vaporization. (c) The evolution of apparent friction with total frictional work. The results from the "*Ref*" case are added for comparison.

interdependent through the Clapeyron relation. This principle has been incorporated into our model (see the verifying model given in Appendix C).

The main drawback of the present model is the assumption of a local thermal equilibrium (LTE) of the system, which means that the pore fluid is invariably at the same macrotemperature as the solid grains in the three regions, liquid, two-phase, and vapor [*Wang and Beckermann*, 1993; *Wang*, 1997]. The assumption of LTE limits the application of the model to temperature differences between solid and liquid and between different solid grains. A detailed description of the heat exchange phenomena during a seismic slip should also incorporate the limitation of heat transfer from the surface to the inside of particles by heat conduction. It should, however, be noted that the present model is not inherently in an equilibrium condition; in fact, the local thermal nonequilibrium (e.g., flash heating at asperities of the contacts) can be readily accounted for, e.g., by using a separate equation for the solid [*Shi and Wang*, 2011]. Efforts in the future could entail the development of a generalized formulation to cover this.

Another drawback is that the pore fluid is modeled as pure water substance, without any dissolved solids and noncondensable gasses. More complex model for nonisothermal flow of water, brine, and volatile compounds (air and CO_2), and including their phase transitions, could be considered in the future.

Moreover, in the present model, convective and dispersive heat transport are neglected, as is appropriate when the fluid flow is relatively slow and when heterogeneities of the porous medium are modeled explicitly [*Rice*, 2006; *Dagan*, 1988]. Future work needs to consider these effects [cf. *Wang*, 1997].

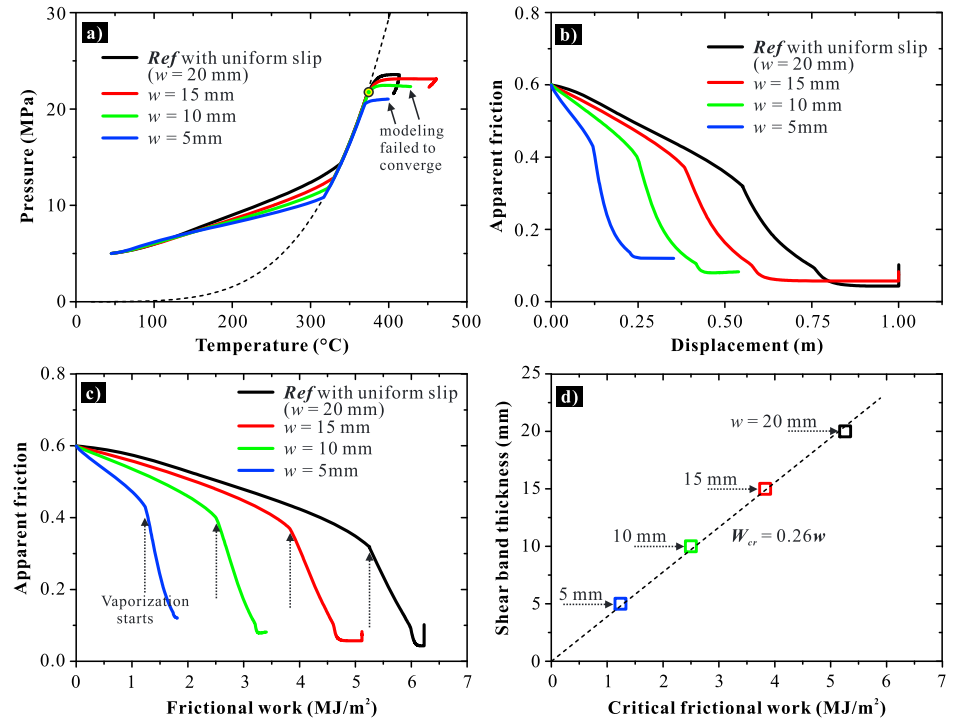## 5.2. A Key Factor Controlling the Onset of Vaporization (If It Occurs)

Referring to the reference case (Figures 6 and 7), our parametric analyses with variable friction coefficients (Figure 8), slip rates (Figure 9), transport properties (Figures 10 and 11), dilatancy effects (Figure 12), localization degrees (Figure 13), and depths (Figure 14) show that the frictional work is the key factor controlling the onset of vaporization and the associated slip weakening and that the critical values (W_{cr}) increase with increasing gouge porosity (φ) and increasing PSZ thickness (w) and are not sensitive to other factors, i.e., friction coefficient (μ_d), sliding velocity (V), and dilatancy effect (reflected by p_{PSZ}). The permeability (k) and

Figure 13. Modeling results of cases with different degrees of slip localization. The results from the "*Ref*" case with uniform slip are added for comparison. (a) The evolution of the PT state of pore fluid at the PSZ center. (b) The evolution of apparent friction with displacement. (c) The evolution of apparent friction with the total frictional work, in which the values of critical frictional work W_{cr} for the onsets of vaporization are indicated by the dash-line arrows. (d) A linear relation exists between W_{cr} and the shear band thickness w, that is $W_{cr} = 0.26w$, where W_{cr} is in a unit of M J/m^2 and w is in millimeter.

depth (z) do not affect W_{cr} either, while as discussed in section 5.3, they have great impacts on whether shear-induced vaporization occurs or not.

Why does the frictional work control the onset of vaporization? To clarify this, we assume that (i) thermal diffusion is negligible during the faulting period (as evident in Figure 6j) and (ii) no chemical reaction is involved ($Q_{ch} = \Omega_{ch} = 0$). Before the onset of vaporization ($Q_{lv} = \Omega_{lv} = S_v = 0$), the energy conservation equation (1) can be simplified as follows:

$$\tau V = w\rho_b c_b \frac{dT}{dt}. \tag{16}$$

Using the mixture properties for the bulk sample (Table 1), equation (16) can be expanded as follows:

$$\tau V = w[\rho_s c_s + \varphi(\rho_l c_l - \rho_s c_s)]\frac{dT}{dt}. \tag{17}$$

Integrating equation (17) over time yields

$$W_f = w[\rho_s c_s + \varphi(\rho_l c_l - \rho_s c_s)]\Delta T. \tag{18}$$

Here W_f is total frictional work done on the gouge and ΔT is the temperature increase. As a first-order approximation, the gouge porosity, the density, and specific heat of pore water (still in a liquid state) are taken as constants in doing the integration, as their variations prior to the occurrence of vaporization are relatively small (less than 4%). Equation (18) indicates that for the pore water to reach the boiling temperature (with the temperature increment referred to as ΔT_{cr}), the critical frictional work (W_{cr}) satisfies the following criterions: (i) it is proportional to the thickness of the shear band w; (ii) it increases linearly with the gouge porosity φ; and (iii) it is insensitive to other parameters, since these factors are either embodied in the expression of the frictional work that $W_f = (\sigma_n - p_{PSZ})\int \mu_d V dt$ (i.e., p_{PSZ}, μ_d, and V) or just not relevant (i.e., k and z). All of these criterions are in satisfactory agreement with our numerical modeling results (Figures 8–14).
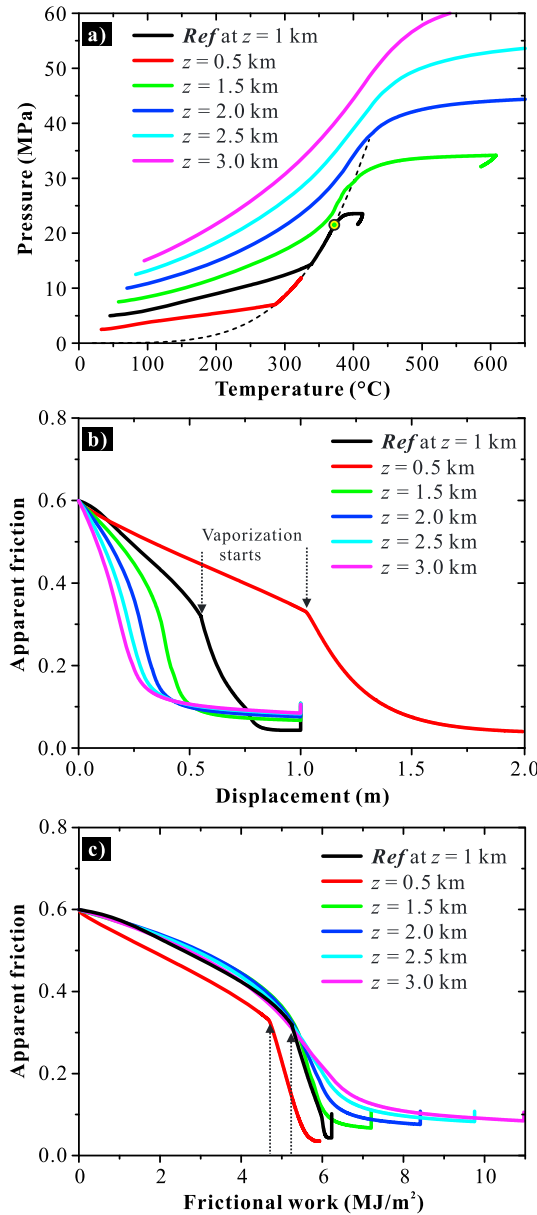
Figure 14. Modeling results of cases at a series of depths from 0.5 to 3 km. (a) The evolution of the PT state of pore fluid at the PSZ center. (b) The evolution of apparent friction with displacement. Note that the transition points to a sharp weakening are only evident when the depths are lower than 1.5 km. (c) The evolution of apparent friction with the total frictional work.

Further, using the ρ_l and c_l values at representative PT conditions along the evolution path ($T = 200\,°C$ and $p = 10$ MPa), we get $\rho_l c_l \approx 15\rho_s c_s$. As such, equation (18) can be reformulated as follows:
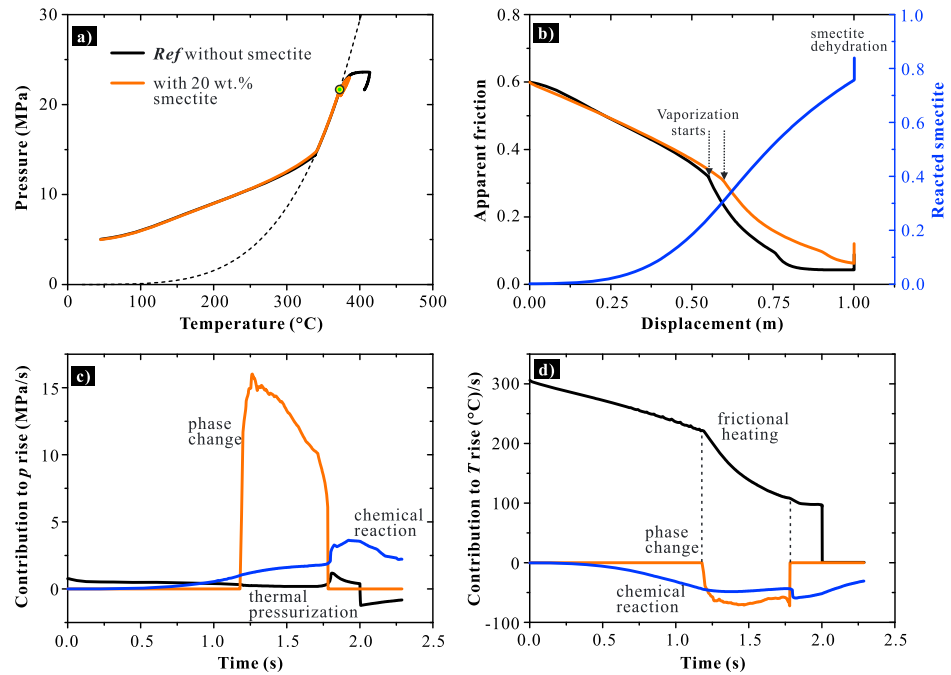
$$W_{cr} = A\varphi + B. \tag{19}$$

Here A ($\approx 15\, w\rho_s c_s \Delta T_{cr}$) specifies the multiplying factor of W_{cr} depending on φ, and B ($= w\rho_s c_s \Delta T_{cr} \approx A/15$) is the intercept W_{cr} value at zero porosity. According to the modeling results, A and B correspond to the slope and the intercept of the fitting curve shown in Figure 11d. Consistently, the fitting equation gives an A/B ratio of ~17. The discrepancy with the value of 15 is acceptable when considering the uncertainty in slope and offset determination.

Reexamining the frictional process before vaporization, we find that the slip velocity (Figure 9), slip zone permeability (Figure 10), and porosity (Figure 11) affect the fluid pressurization rate (dp/dt) little and thus have little effect on the evolution of apparent friction, whereas the friction coefficient (Figure 8), initial pore pressure (or dilatancy, Figure 12), slip band thickness (Figure 13), and depth (Figure 14) do. Recall that before the onset of vaporization, the pore pressure rise is fully due to TP which occurs within a very short time (<1.1 s as in the reference case, Figure 6). Following *Mase and Smith* [1987], the hydraulic diffusivity (D_h) and thermal diffusivity (D_t) during a TP process can be written as $D_h = k/(\eta_f S_s)$ and $D_t = K_b/(\rho_b c_b)$, respectively. In a given time scale (t), the hydraulic and thermal diffusivity length (L_h and L_t) are defined as follows:

$$L_h = (D_h t)^{1/2} \tag{20}$$

$$L_t = (D_t t)^{1/2}. \tag{21}$$

Using typical values for fluid viscosity ($\eta_f = 6.0 \times 10^{-4}$ Pas), permeability ($k = 1.2 \times 10^{-16}$ m^2), specific storage ($S_s = 6.1 \times 10^{-9}$ Pa^{-1}), thermal conductivity ($K_b = 2.6$ Wm^{-1} K^{-1}), density ($\rho_b = 2405.8$ kg m^{-3}), and specific heat capacity ($c_b = 409.9$ J kg^{-1} K^{-1}) of the bulk gouge from the PSZ, for a diffusion time of 1.1 s, we obtain L_h and L_t of 6.0 mm and 1.7 mm, respectively. Both L_h and L_t are less than half of the PSZ thickness ($20/2 = 10$ mm). Therefore, the slip can be considered to be under adiabatic and undrained conditions. Following the analytical solution given by *Rice* [2006], the evolution of shear stress with displacement (L) can be calculated as (his equation (16)):

$$\tau(L) = \mu_d(\sigma_n - p) = \mu_d(\sigma_n - p_{PSZ})\exp\left(-\frac{\Lambda}{\rho_b c_b}\frac{\mu_d}{w}L\right), \tag{22}$$

Figure 15. Modeling results of the case in which the fault gouge is assumed to contain 20 wt % smectite. The results from the "*Ref*" case are added for comparison. (a) The evolution of the PT state of pore fluid at the PSZ center. (b) The evolution of apparent friction and reacted reactant (smectite) with displacement. Note that in this case the onset of vaporization is slightly delayed by the reaction. (c) Comparison of the fluid pressurization attributed to thermal pressurization, chemical reaction, and the phase change. (d) Comparison of the temperature rises caused by frictional heating, chemical reaction, and the phase change.

where Λ is thermal pressurization coefficient, defined as $\Lambda = \varphi(\alpha_f - \alpha_s)/S_s$. (by using the approximation $S_s \approx \varphi(\beta_f + \beta_\varphi)$, Λ can be rewritten as $\Lambda = (\alpha_f - \alpha_s)/(\beta_f + \beta_\varphi)$). Assuming constant fluid and rock properties ($\Lambda/\rho_b c_b$), it is apparent from equation (22) that the evolution of shear stress depends on the friction coefficient (μ_d), shear band thickness (w), initial pore pressure (p_{PSZ}), and depth (reflected by σ_n), which is fully consistent with our numerical observations (see Figures 8 and 12–14). This equation (22) also explains why slip velocity, permeability, and porosity do not affect the shear stress evolution for the early stage of the slip (Figures 9–11).

Finally, it should be noted that all the frictional work is assumed to have been converted to heat in the present model, while it is the frictional heat E_T, in natural earthquakes, that controls the onset of vaporization (part of the work that dissipates through heat). For a 2 cm thick slip zone with a typical porosity of 5%–40% [*Wibberley and Shimamoto*, 2005; *Tanikawa et al.*, 2009, 2013; *Chen et al.*, 2013; *Morrow et al.*, 2014], our modeling shows that the heating that is required to stimulate vaporization falls in the range of 2.5–10.0 M J/m^2 (Figure 11d). Field observations indicated that shear deformation in major earthquakes is often confined to slip bands that are on the order of 100 μm wide or even less [e.g., *Rice et al.*, 2014], which would reduce the W_{cr} value down to 0.013–0.05 M J/m^2. These values are much lower than either the frictional heat estimated from HVF curves of fault gouges (e.g., 1–12 M J/m^2) [*Mizoguchi et al.*, 2007a; *Togo and Shimamoto*, 2012] or the seismological estimates of natural large earthquakes (1–100 M J/m^2) [*Rice*, 2006]. Therefore, the energy consumption for the activity of vaporization can easily be achieved in earthquakes.

5.3. Combined Roles of Variable Fluid Pressurization Processes
5.3.1. Vaporization Versus Thermal Pressurization (TP)
Our modeling of the reference case and the parametric analyses (Figures 6–14) indicate that shear-induced vaporization can occur prevailingly in a typical natural earthquake at shallow depths (e.g., 1 km). The variations in all the parameters investigated can only delay or advance the occurrence of vaporization (μ_d, V, φ, p_{PSZ}, and w) and occasionally alter the pressurization effect (e.g., μ_d). Generally, its occurrence is following

a slip time, during which pure thermal expansion of pore fluid (TP) initially controls the slip weakening. Once vaporization occurs, the pore pressure will increase rapidly, leading to a sharp slip weakening superimposed on the weakening by TP. The pressure rise due to vaporization appears to be more pronounced than that caused by TP (Figure 6), at least for the fault configuration considered in the present study. A strong evidence for this is that lower steady state apparent frictions are predicted at shallower depths of a fault with the occurrence of vaporization (Figure 14). Our parametric analyses further show that as the slip zone gets less permeable and/or the fault is deeper, TP will become more efficient and the PT state might not meet the SVC (Figures 10a and 14a). In the following, we discuss how these parameters (permeability and depth) affect vaporization under realistic conditions.

In this study, the permeability data used were from the Chelungpu fault, where the gouge permeability varies from 3×10^{-17} to 2×10^{-15} m^2 at 0.5–3 km depths (Figure 5). We noticed that at similar levels, the permeabilities of natural fault gouges can vary over a much wider range, as in the Nojima fault (1×10^{-18}–3×10^{-14} m^2) [*Mizoguchi et al.*, 2008], the plate boundary fault, Japan (~10^{-20}–10^{-18} m^2) [*Tanikawa et al.*, 2013], and the Longmenshan fault, China (2×10^{-18}–3×10^{-14} m^2; 4×10^{-19}–2×10^{-18} m^2) [*Chen et al.*, 2011, 2013]. Notably, by varying the gouge permeability by 4 orders of magnitude, our modeling indeed reveals that vaporization can be inhibited by the counterpart TP process in the case of low permeability, in which the pore pressure rises so fast that the pore water cannot vaporize much before entering the supercritical state (Figure 10a). Nonetheless, we believe that low permeability is not an issue for the activation of vaporization at shallow depths of an earthquake fault (~1 km), for the following reasons: (i) The transport properties of fault rocks, including the above mentioned, were usually measured at hydrostatic pressure conditions, while the permeabilities during a dynamic rupture process are expected to be much higher due to the dilatant effect [e.g., *Segall and Bradley*, 2012]. (ii) Our modeling results show that even at low permeabilities of the order of 10^{-20}–10^{-19} m^2 ($k = 0.001\,k_1$), vaporization can still occur at the modeled condition (Figure 10).

Interestingly, in the case of low gouge permeabilities, after entering the subcritical region where vaporization does not occur, the PT state of pore water still evolves along the extension cord of the SVC (Figure 10a). Similar behavior is also predicted in the cases at depths greater than 1.5 km, in which the PT states of pore water do not meet the SVC but the evolution curves appear to move along the extension cord of the SVC (Figure 14a). We infer that this sort of behavior is due to the rapid change of the thermophysical properties of water. As shown in Figures 2a and 2b, in the supercritical region beyond the critical point, the contour maps of density and enthalpy exhibit a large density of contour lines (in equal intervals), suggesting rapid changes in the derived properties of enthalpy and density, such as thermal expansivity ($\alpha = -(\partial\rho/\partial T)_p/\rho$), compressibility ($\beta = (\partial\rho/\partial p)_T/\rho$), and specific heat capacity ($c = [\partial(\rho h)/\partial T]_p/\rho$) [*Chen et al.*, 2013] (also, refer to the NIST database). Below the critical point ($T < 374°C$), it is the discontinuities of these properties along the saturated vapor curve (ρ, h, α, β, and c, as well as K and η) that promote fluid pressurization and endothermic effects associated with the phase transition. We propose that the rapid, continuous changes of these properties in the supercritical region can contribute to similar effects, preventing the pore water from crossing this region.

5.3.2. Vaporization Versus Thermochemical Pressurization (TCP)

As reflected by the terms in the equations (Q_{lv} versus Q_{ch}, Ω_{lv} versus Ω_{ch}, and $\kappa_{l\text{-}v}(p, T)$ versus $\kappa(T)$), shear-induced phase transition and thermochemical pressurization (TCP) have similarities in terms of the endothermic effect, the pressurization effect, and their thermally activated nature. Compared to a decomposition reaction, a phase transition has the following characteristics.

First, the phase transition of water is an internally reversible process, which implies that with the occurrence of vaporization, the reverse, condensation process could also occur when the seismic slip is terminated. Due to this characteristic, the frictional heat that is stored in the heated vapor phase during shearing will be released by condensation in the postseismic period. This is different from mineral phase transitions, e.g., dehydration and decarbonation [*Brantut et al.*, 2010; *Sulem and Famin*, 2009], in which heat is permanently stored in the reaction products, as the reverse reactions (rehydration and recarbonation) are practically irreversible, due to the slow kinetics and/or the absence of sufficient volatiles to rehydrate or recarbonate the entire slipping zone.

Second, as restrained by the Clapeyron relation, both vaporization and condensation can proceed with infinite transition rates and over a wide range of temperatures (100–374°C) depending on the in situ pressures,

while the shear-induced reactions that have been reported in literature (e.g., *dehydration* of smectite, kaolinite, gypsum, talc, and serpentine (antigorite, lizardite, and chrysotile); *dehydroxylation* of illite and dehydrated smectite, and *decarbonation* of dolomite, calcite, and siderite), have specific reaction kinetics, as embedded by the reaction rate constants (A_i), the activation energies (E_i), and the equilibrium reaction temperatures [e.g., *Sulem and Famin*, 2009; *Brantut et al.*, 2010].

Finally, in terms of the content of "reactant," water is more abundant at shallow depths of fault zones compared with most of the above mentioned minerals. Note that for some reactions, the dehydrated water can also vaporize, depending on the equilibrium temperature of the reactions versus the boiling temperature. At shallow crustal depths ($<$3 km), the porosity, which contains the free water, generally falls in the range from 5% to 40% for the PSZ gouges collected from seismically active faults (e.g., at P_e of ~15 MPa, the porosities are 6.5% for the Median Tectonic Line fault, Japan [*Wibberley and Shimamoto*, 2005]; 17.3% for the Chelungpu fault, Taiwan [*Tanikawa et al.*, 2009]; 25% for the plate boundary fault, Japan [*Tanikawa et al.*, 2013]; ~15% for the Longmenshan fault, China [*Chen et al.*, 2013]; and more than 5%–9% for the San Andreas Fault, USA [*Morrow et al.*, 2014]). In contrast, the amount of water that could be liberated by dehydration reactions from a fault gouge is usually lower than these values. The mass of released water per unit volume of a fault gouge can be calculated from the stoichiometry of the reaction and the amount of hydrous mineral within the fault volume. Take the Japan Trench fault gouge, for instance, which is extremely enriched in smectite (up to 80%) [*Kameda et al.*, 2015] and has a porosity of ~25% [*Tanikawa et al.*, 2013]. Provided that the smectite carries one interlayer water in its unit cell [*Chen et al.*, 2013; *Schleicher et al.*, 2015], only 5.0 vol % of water can be released per unit volume of the gouge (calculated as $\Pi_{sm}\omega_{sm}(1-\varphi)$, where ω_{sm} is 80%, φ is 25%, and Π_{sm} is 8.2% for smectite; equation (7) and Table 2). Even in this case, the water contained in the gouge is much less than the free water enclosed in the pore space (25%), not to mention that the dehydrated water can also vaporize (smectite dehydrates at ~80°C). There are indeed some hydrous minerals that contain high contents of water, such as the serpentine family which are developed in natural fault zones like the San Andreas Fault [e.g., *Moore and Rymer*, 2007]. Take lizardite, for instance, which has a typical composition of $(Mg)_3(Si_2O_5)(OH)_4$, with a molar mass of 296 g/mol and a density of 2.5 g/cm^3. Following the reaction that 5lizardite→talc + 6forsterite + 9H$_2$O, dehydration of lizardite can release 10.9 wt % of free water which corresponds to 27.3 vol % (assuming no porosity is created) [*Brantut et al.*, 2011a]. However, considering the fact that serpentine only appears as minor or trace mineral(s) in the lithology of the fault gouges (2%–8% by *Moore and Rymer* [2007], a trace amount by *Zoback et al.* [2011], and less than 10% by *Bradbury et al.* [2011]) and that the equilibrium temperature of the reaction is relatively high ($>$550°C) [*Brantut et al.*, 2010], the importance of this reaction is limited, at least at shallow depths of the fault. At greater depths, dehydration of serpentine may play an important role in dynamic fault lubrication and rupture propagation [*Brantut et al.*, 2016], especially for subduction fault zones where serpentine is expected to be abundant by the hydration of olivine (with an optimum hydration rate at ~300°C) [*Reynard*, 2013].

In the present study, the dehydration of smectite is taken as an example of TCP. The results show that the reaction can delay the onset of vaporization (Figure 15b) and we infer that this is because smectite dehydrates at ~80°C, lower than the boiling temperature of water (Figure 15a). With the occurrence of both dehydration and vaporization, they can both help build up the pore pressure, but meanwhile, they compete with one another, with the early activated process inhibiting the other. Though detailed work involving other reactions is needed, our limited results indicate that vaporization can produce more effective fluid pressurization than a chemical reaction due to its faster kinetics and the larger amount of reactant (Figure 15c). It is noteworthy that in the present model, we have neglected changes in porosity and permeability from the dynamic mechanical deformation during an earthquake. Though the incipient dilatancy has been taken into account by varying the initial pore pressure, the dilatancy and/or compaction with the successive slip could also affect the fluid pressure evolution. Rigorous modeling of fluid pressurization during seismic slip is needed in the future to cover this effect (through the term $-\mathrm{d}\varphi_d/\mathrm{d}t$ in equation (5)).

5.4. Implications for Natural Earthquakes

Following the above considerations, we believe that shear-induced vaporization of pore water can play an important role in natural earthquakes, at least for those large enough to produce coseismic ruptures that propagate to the shallow levels of the crust. It may have the following effects.

The dynamic slip weakening associated with large earthquakes can be contributed to pore fluid pressurization due to thermal pressurization, thermochemical pressurization, and vaporization. Though TP (or TCP) has been widely accepted to be the dominant slip-weakening mechanisms, it has been proposed that it can be strongly suppressed by dilatancy [e.g., *Segall and Bradley*, 2012; *Urata et al.*, 2013], and its importance can be further questioned for the shallow portions of the faults, where the gouge permeability is relatively high [e.g., *Wibberley and Shimamoto*, 2005; *Mizoguchi et al.*, 2008; *Chen et al.*, 2011]. Our results show that slip weakening by vaporization can still be significant even when the gouge has a high permeability of the order 10^{-15}–10^{-14} m^2 ("$k = 10\ k_1$," Figure 10). Therefore, the combination of TP and vaporization of pore water, perhaps with decomposition reactions, can provide an appealing explanation for the slip weakening or low shearing resistance observed in the shallow portions of a fault. Previous studies have investigated the roles TP and TCP play during a dynamically propagating earthquake slip [*Andrews*, 2002; *Garagash and Rudnicki*, 2003; *Bizzarri and Cocco*, 2006; *Noda and Lapusta*, 2010, 2013; *Brantut et al.*, 2011a; *Segall and Bradley*, 2012; *Garagash*, 2012; *Urata et al.*, 2013; *Platt et al.*, 2015]. With faster "reaction kinetics" and larger content of the reactant, the change in fluid pressure and/or system stiffness by vaporization is expected to lead to a change in the slip velocity, i.e., to a sudden acceleration of the fault [e.g., *Andrews*, 2002; *Scholz*, 2002]. Additional effects of vaporization, similar to those relevant to TP (or TCP), include a reduction in fracture energy and frictional heat [*Wibberley and Shimamoto*, 2005], an accelerated rupture velocity, and a prolonged slip distance [*Bizzarri and Cocco*, 2006; *Rice*, 2006]. Recent modeling studies are now leading to an improved understanding of the coseismic frictional heating and fluid pressurization processes and of their influence on fault rupture propagation [e.g., *Noda and Lapusta*, 2013]. Other recent studies also show that the operation of a thermal or chemical (weakening) process plays an important role in the generation of localized shear bands [*Platt et al.*, 2014, 2015; *Sulem and Stefanou*, 2016], compared with distributed slip, which can lead to slip acceleration and in turn enhance frictional heating. It is important for these models to also include the shear-induced vaporization process and the associated strain localization effect. Finally, vaporization might even lead to a violent escape of highly pressured fluids away from the slip zone, depending on the sealing conditions of the faults. Huge rock eruptions have been reported at Chiu-Fen-Erh-Shan during the 1999 Chi-Chi earthquake and are inferred to be due to the high vapor pressure generated by frictional heating during seismic slip [*Huang et al.*, 2003].

Besides the fluid pressurization effect, the phase transition of pore water also has a significant endothermic effect [*Kitajima et al.*, 2010; *Brantut et al.*, 2011b]. Our study shows that at local thermal equilibrium, the occurrence of vaporization could buffer the macrotemperatures of the fault gouge to not exceed the boiling temperatures (Figures 6–14). This is consistent with our recent HVF experiments [*Chen et al.*, 2017], in which we observed that with the presence of liquid water, the macrotemperatures of the gouge layer subjected to frictional heating did not surpass the boiling temperatures—except when the water had completely escaped the slipping zone. This temperature buffering effect may explain why low-temperature anomalies were measured in the principal slip zones of large earthquakes at 0.3–0.6 km borehole depths in drilling campaigns (e.g., the 1999 Chi-Chi earthquake on the Chelungpu fault [*Tanaka et al.*, 2006] and the 2008 Wenchuan earthquake on the Longmenshan fault [*Li et al.*, 2015]). At these depths, vaporization, if it occurs, could keep the macrotemperatures of the slip zones lower than expected in the absence of vaporization. According to the phase diagram of water (Figure 3) and assuming hydrostatic pressure conditions at these depths (<0.6 km), vaporization is expected to occur if the local temperatures on the slip surfaces reach the critical value of less than 276°C (at a pore pressure of 6 MPa). This critical value can be higher if we consider a higher pore pressure caused by thermal or thermochemical pressurization, but, at the same time should be lower than 343°C which would correspond to a pore pressure equal to the lithostatic pressure (<15 MPa). In fact, as constrained from various temperature proxies (fission tracks, reaction kinetics, magnetic analysis, and trace elemental and isotopic analyses, as well as Raman spectra, vitrinite reflectance, and biomarkers of carbonaceous materials) [e.g., *Mishima et al.*, 2006; *Hirono et al.*, 2006, 2015; *Sakaguchi et al.*, 2007; *Ishikawa et al.*, 2008; *Hamada et al.*, 2009; *Otsuki et al.*, 2009; *Kuo et al.*, 2011; *Savage et al.*, 2014; *Yang et al.*, 2016], much higher temperatures (>276°C) have been reported for the slip zones associated with the aforementioned earthquakes. Taking the 1999 Chi-Chi earthquake, for example, where the principal fault slip occurred at ~300 m depth in the Chelungpu scientific drilling [*Tanaka et al.*, 2006], magnetic analysis of the slip materials within the core samples indicated that the slip zones have experienced temperatures of at least 400°C

[*Mishima et al.*, 2006], which is consistent with the temperatures obtained by using the compositions of major and trace elements (>350°C by *Ishikawa et al.* [2008]), inorganic carbon content (550°C by *Hirono et al.* [2006]), and vitrinite reflectance geothermometry (400–626°C by *Maekawa et al.* [2014]), as well as infrared and Raman spectroscopies (~700°C by *Hirono et al.* [2015]). The questions then are how extensive vaporization would be during a natural earthquake and how its operation would affect the method for determining the dynamic friction from temperature logging data in boreholes shortly after an earthquake. Similar concerns would also need to be addressed for the HVF experiments, especially when slip zone temperatures were estimated from the friction curve and used to infer the deformation or slip-weakening mechanism [e.g., *Ujiie et al.*, 2013].

It is noteworthy that the phase transition of pore water is a reversible process so that the frictional heat stored in the heated vapor phase during a coseismic period will be released by condensation in the postseismic period but likely over a larger space and time (because of hydraulic diffusion). In terms of the energetic effects, vaporization can, as discussed above, lead to less frictional heat being generated due to fluid pressurization, while the latent heat, due to the reversible characteristics, does not contribute to the energy budget at all, although it can reduce the maximum temperature seismically experienced by the slip surface.

The above analyses have addressed the possibility and the effects of the occurrence of vaporization at around 1 km depth during an earthquake. Our simulations further show that the phase transition of pore water can be of great influence to at least 3 km depth, due to the rapid changes of fluid properties in the supercritical region (Figure 14). Finally, we re-emphasize that vaporization can occur at even deeper levels but in a different scenario [*Weatherley and Henley*, 2013]. At these greater depths, crack growth or openings that develop at an early stage of an earthquake will result in a sudden drop in the pore fluid pressure, which might bring the PT state directly to meet the SVC (Figure 3). With successive displacement, the vaporized pore water will then move along the SVC, similar to the scenario modeled in the present study. Considering a critical-point temperature of 374°C, this depressed vaporization process can play a role up to ~15 km (assuming a geothermal gradient of 25°C/km).

6. Conclusions

In this study, we incorporated a two-phase mixture model in simulations of the thermo-hydro-chemo-mechanical processes in a water-saturated fault zone during an earthquake, including frictional heating, thermal pressurization, chemical reaction(s), and phase transitions of pore water. Employing fault zone structure and parameters from a typical seismogenic fault (i.e., the Chelungpu fault), our simulations of earthquake slip indicate that pore water vaporization can readily occur at shallow crustal levels of a fault (e.g., 1 km), irrespective of the variations of other parameters, such as friction coefficient, slip velocity, shear localization, gouge permeability, and gouge porosity, as well as shear-induced dilatancy. Upon vaporization, the pore fluid evolves along the liquid-to-vapor phase transition curve in the pressure-temperature phase diagram, giving rise to a transition to a sharp slip weakening, superimposed on the weakening by thermal and thermochemical pressurization. The frictional work is the key factor that controls the onset of vaporization. Applied to natural earthquakes, our results indicate that the propagation of large earthquakes into the shallow crust could be facilitated by water vaporization. The fluid pressurization and temperature buffering effects associated with the phase transition can also provide an alternative explanation for the fact that low thermal anomalies were measured in the principal slip zones at shallow depths of large earthquakes.

Appendix A: Two-Phase Mixture Model for Coseismic Energy Conservation

The equation governing temperature evolution during a seismic slip can be obtained from the total energy conservation for a solid-liquid-vapor multiphase mixture system and by assuming local thermodynamic equilibrium. The energy conservation can be expressed in terms of enthalpy (*h*), that is,

$$\frac{\partial(\rho_b h_b)}{\partial t} + \nabla\cdot(\rho_f \mathbf{u_f} h_f) = \nabla\cdot(K_b \nabla T) + Q. \tag{A1}$$

In (A1), ρ_b and h_b are the density and enthalpy of the combined three-phase system in the units of kg/m³ and J/kg, respectively; K_b is the effective thermal conductivity (Wm^{-1} K^{-1}), and Q is the external heat source/sink

in unit volume of the gouge (J m^{-3} s^{-1}). The second term specifies the heat advection by fluid flow, where $\mathbf{u_f} = (u_l, u_v)$ is the Darcy velocity of the fluid (u_l and u_v for the liquid and vapor phases, respectively), and ρ_f and h_f are the density and enthalpy of the two-phase mixture of fluid, respectively. Due to the small quantity, this advection term is usually neglected in modeling a coseismic slip [*Rice*, 2006]. In the following derivations, quantities with subscripts l and v denote liquid and vapor properties, respectively, while the subscript "f" is reserved for the two-phase mixture of pore fluid and b for the bulk sample. All the symbols and subscripts used in this study are explained in the nomenclature.

From the properties of individual phases, we have mixture properties for the pore fluid and the bulk sample. They are described as the function of the relative volume fractions of liquid and vapor phases (S_l and S_v), and of the gouge porosity (φ), as follows,

$$
\begin{aligned}
\rho_f &= S_l\rho_l + S_v\rho_v \\
\rho_f h_f &= S_l\rho_l h_l + S_v\rho_v h_v \\
K_f &= S_l K_l + S_v K_v
\end{aligned}
\tag{A2a}
$$

and

$$
\begin{aligned}
\rho_b &= (1-\varphi)\rho_s + \varphi\rho_f = (1-\varphi)\rho_s + \varphi S_l\rho_l + \varphi S_v\rho_v \\
\rho_b h_b &= (1-\varphi)\rho_s h_s + \varphi\rho_f h_f = (1-\varphi)\rho_s h_s + \varphi S_l\rho_l h_l + \varphi S_v\rho_v h_v. \\
K_b &= (1-\varphi)K_s + \varphi K_f = (1-\varphi)K_s + \varphi S_l K_l + \varphi S_v K_v
\end{aligned}
\tag{A2b}
$$

The enthalpies in (A2a) and (A2b) are related to temperature by

$$
\begin{aligned}
h_s &= c_s T + h_{s0} \\
h_l &= c_l T \\
h_v &= c_v T + [(c_l - c_v)T_{SVC} + \Delta h_{lv}].
\end{aligned}
\tag{A3}
$$

Here h_{s0} is the solid enthalpy at zero K, T_{SVC} is the boiling temperature of the phase transition, and Δh_{lv} is the latent heat, expressed as $\Delta h_{lv} = h_v - h_l \mid_{T=T_{SVC}}$. From (A3) and the definition that $\rho c = \mathrm{d}(\rho h)/\mathrm{d}T$, we have

$$
\begin{aligned}
\rho_f c_f &\equiv \frac{\partial(\rho_f h_f)}{\partial T} = S_l\rho_l c_l + S_v\rho_v c_v \\
\rho_b c_b &\equiv \frac{\partial(\rho_b h_b)}{\partial T} = (1-\varphi)\rho_s c_s + \varphi\rho_f c_f.
\end{aligned}
\tag{A4}
$$

The first term in (A1) can be obtained by differentiating its product:

$$
\frac{\partial(\rho_b h_b)}{\partial t} = \frac{\partial(\rho_b h_b)}{\partial T}\frac{\partial T}{\partial t} + \frac{\partial(\rho_b h_b)}{\partial S_v}\frac{\partial S_v}{\partial t}.
\tag{A5}
$$

Note that the changes in porosity (φ) and specific heat (c_l and c_v) should also have effects on influencing the enthalpy change of the system. Considering the small quantities, the partial differential products with respect to these variables are neglected on the right side of (A5). As given above (A4), the derivative term $\partial(\rho_b h_b)/\partial T$ appearing in equation (A5) specifies the heat storage per unit volume:

$$
\frac{\partial(\rho_b h_b)}{\partial T} = \rho_b c_b.
\tag{A6}
$$

The phase transition of pore water in each increment of time can be considered as an isothermal process ($T = T_{SVC}$) in which a given mass/volume of liquid water is replaced by vapor water (or in the reverse direction). As such, the second derivative term on the right-hand side of (A5) can be expressed as follows:

$$
\frac{\partial(\rho_b h_b)}{\partial S_v} = \varphi\rho_l\Delta h_{lv}.
\tag{A7}
$$

Note that in (A7), variation in liquid phase density (ρ_l) is neglected, as is appropriate for (nearly) isothermal conditions in the iteration step.

As addressed in the main text, the frictional work by an earthquake is assumed to be distributed among frictional heating, chemical reactions, and phase transition. The latent heat associated with a phase

transition has been included in the above analysis. The external heat source/sink (Q in equation (A1)) thus consists of the frictional heat (Q_{fr}) and the endothermic heat (Q_{ch}) of the involved chemical reaction(s), that is,

$$Q = Q_{fr} + Q_{ch}. \tag{A8}$$

Substituting (A5)–(A8) into (A1), we have the energy conservation equation:

$$\rho_b c_b \frac{\partial T}{\partial t} + \varphi \rho_l \Delta h_{lv} \frac{\partial S_v}{\partial t} = \nabla \cdot (K_b \nabla T) + Q_{fr} + Q_{ch}. \tag{A9}$$

To be consistent with a reaction, we define the enthalpy change of a phase transition in a unit of per molar and negative for an endothermic process, that is, $\Delta H_{lv} = -\Delta h_{lv} M_{H2O}$.

Finally, the energy balance equation (A9) can be reformulated as follows:

$$\rho_b c_b \frac{\partial T}{\partial t} = \nabla \cdot (K_b \nabla T) + Q_{fr} + Q_{ch} + Q_{lv}, \tag{A10}$$

where $Q_{lv} = \varphi \rho_l \frac{\Delta H_{lv}}{M_{H2O}} \cdot \frac{\partial S_v}{\partial t}$. In this equation, Q_{fr}, $Q_{ch,}$ and Q_{lv} are the thermal effects related to frictional heating, chemical reactions, and phase transition of pore water, respectively. The constitutive relations for the *bulk* sample properties (with subscript b) are given in equations (A2a), (A2b), (A3), and (A4) (see also Table 1).

Appendix B: A Two-Phase Mixture Model for Coseismic Fluid Mass Conservation

Conservation of fluid mass for liquid and vapor phases can be expressed by

$$\frac{\partial(\varphi S_l \rho_l)}{\partial t} + \nabla \cdot (\rho_l u_l) = \frac{\partial m_l}{\partial t}$$
$$\frac{\partial(\varphi S_v \rho_v)}{\partial t} + \nabla \cdot (\rho_v u_v) = \frac{\partial m_v}{\partial t}, \tag{B1}$$

where $\varphi S_l \rho_l$ and $\varphi S_v \rho_v$ are the total mass of liquid and vapor phases per unit volume of the gouge (in a reference state), the second terms are the mass flux of the liquid and vapor phases out of the unit volume, and m_l and m_v are the fluid mass sources/sinks for the liquid and vapor phases, respectively, which may arise due to internal phase transition or chemical reactions. S_l and S_v define the fractions of the liquid and vapor phases in the pore volume, respectively (Figure 1).

1. The first term of equation (B1) can be obtained by differentiating this product:

$$\frac{\partial(\varphi S_l \rho_l)}{\partial t} = S_l \rho_l \frac{\partial \varphi}{\partial t} + \varphi S_l \frac{\partial \rho_l}{\partial t} + \varphi \rho_l \frac{\partial S_l}{\partial t}$$
$$\frac{\partial(\varphi S_v \rho_v)}{\partial t} = S_v \rho_v \frac{\partial \varphi}{\partial t} + \varphi S_v \frac{\partial \rho_v}{\partial t} + \varphi \rho_v \frac{\partial S_v}{\partial t}. \tag{B2}$$

The first two derivative terms appearing on the right-hand side of (B2) are given by the following:

$$\frac{\partial \varphi}{\partial t} = \frac{\partial \varphi}{\partial p} \frac{\partial p}{\partial t} + \frac{\partial \varphi}{\partial T} \frac{\partial T}{\partial t} + \frac{\partial \varphi_p}{\partial t} = \varphi \beta_p \frac{\partial p}{\partial t} + \varphi \alpha_p \frac{\partial T}{\partial t} + \frac{\partial \varphi_p}{\partial t} \tag{B3}$$

and

$$\frac{\partial \rho_l}{\partial t} = \frac{\partial \rho_l}{\partial p} \frac{\partial p}{\partial t} + \frac{\partial \rho_l}{\partial T} \frac{\partial T}{\partial t} = \rho_l \beta_l \frac{\partial p}{\partial t} - \rho_l \alpha_l \frac{\partial T}{\partial t}$$
$$\frac{\partial \rho_v}{\partial t} = \frac{\partial \rho_v}{\partial p} \frac{\partial p}{\partial t} + \frac{\partial \rho_v}{\partial T} \frac{\partial T}{\partial t} = \rho_v \beta_v \frac{\partial p}{\partial t} - \rho_v \alpha_v \frac{\partial T}{\partial t}, \tag{B4}$$

where $\alpha_p = (\partial \varphi / \partial T)_p / \varphi$, $\alpha_l = -(\partial \rho_l / \partial T)_p / \rho_l$, and $\alpha_v = -(\partial \rho_v / \partial T)_p / \rho_v$ are thermal expansivities; $\beta_p = (\partial \varphi / \partial p)_T / \varphi$, $\beta_l = (\partial \rho_l / \partial p)_T / \rho_l$, and $\beta_v = (\partial \rho_v / \partial p)_T / \rho_v$ are compressibility of the pore volume, the liquid phase, and the vapor phase, respectively. Usually, the thermal expansivity of pore volume (α_p) takes the thermal expansion coefficient of the solid grains for thermoporoelastic materials (α_s). These are all known properties (either constant or PT state dependent, Table 2).

In equation (B3), $\partial\varphi_p/\partial t$ is the rate of inelastic porosity change [*Garagash and Rudnicki*, 2003]. For a granular material under shear, it is attributed to either the shear-induced dilatancy or chemical reactions [*Sulem and Famin*, 2009], that is,

$$\partial\varphi_p/\partial t = \partial\varphi_d/\partial t + \partial\varphi_{ch}/\partial t, \tag{B5}$$

where $\partial\varphi_d/\partial t$ is the so-called "dilatancy rate" [*Marone et al.*, 1990] and $\partial\varphi_{ch}/\partial t$ is the rate of the porosity change by chemical reaction(s) and can be related to the reaction kinetics ($\partial\xi_i/\partial t$) as follows:

$$\frac{\partial\varphi_{ch}}{\partial t} = \Sigma\omega_i(1-\varphi)\Delta V_i\frac{\partial\xi_i}{\partial t}. \tag{B6}$$

Here Σ represents the summation of all involved reactions, ω_i and ΔV_i are the mass content and specific solid volume shrinkage of the reactant (i) contained in the gouge, and ξ_i is the accumulative reacted mass fraction of the reactant (see definition in the main text).

Using equations (B2)–(B6), the first term of equation (B1) can be therefore written as follows:

$$\frac{\partial(\varphi S_l\rho_l)}{\partial t} = \varphi S_l\rho_l\left[(\beta_p+\beta_l)\frac{\partial p}{\partial t} - (\alpha_l-\alpha_s)\frac{\partial T}{\partial t}\right] + S_l\rho_l\left(\frac{\partial\varphi_{ch}}{\partial t} + \frac{\partial\varphi_d}{\partial t}\right) + \varphi\rho_l\frac{\partial S_l}{\partial t}$$
$$\frac{\partial(\varphi S_v\rho_v)}{\partial t} = \varphi S_v\rho_v\left[(\beta_p+\beta_v)\frac{\partial p}{\partial t} - (\alpha_v-\alpha_s)\frac{\partial T}{\partial t}\right] + S_v\rho_v\left(\frac{\partial\varphi_{ch}}{\partial t} + \frac{\partial\varphi_d}{\partial t}\right) + \varphi\rho_v\frac{\partial S_v}{\partial t}. \tag{B7}$$

2. The second terms in (B1) are fluid flux by Darcy flow, which can be expressed by the relationships of flow velocities with phase pressures:

$$u_l = -k\nabla p_l\cdot(k_{rl}/\eta_l)$$
$$u_v = -k\nabla p_v\cdot(k_{rv}/\eta_v), \tag{B8}$$

where k is the intrinsic permeability of the sample independent of fluid media and p_l and p_v are the partial pressures for liquid and water phases, respectively. Further, k_{rl}, k_{rv}, η_l, and η_v are the relative permeabilities and dynamic viscosities of liquid and vapor phases, respectively. When capillary pressure is negligibly small, we have $p = p_l = p_v$.

3. The mass sources/sinks in equation (B1) include two parts, namely, the phase transition and chemical reaction (i.e., dehydration, dehydroxylation, and decarbonation). For the sake of simplicity, in the present model, we only consider the dehydration reaction and assume that water is released from the hydrates in the liquid state. The mass change rates of liquid and vapor water can be thus expressed as follows:

$$\frac{\partial m_l}{\partial t} = \frac{\partial m_{lv}}{\partial t} + \frac{\partial m_{ch}}{\partial t}$$
$$\frac{\partial m_v}{\partial t} = -\frac{\partial m_{lv}}{\partial t} \tag{B9}$$

In (B9), m_{lv} specifies the mass that is involved in an internal phase transition process. In the absence of any external mass source or sink (e.g., reaction), we have $\partial m_l/\partial t + \partial m_v/\partial t = 0$. Following *Chen et al.* [2013], the mass change rate by chemical reactions can be expressed as follows:

$$\frac{\partial m_{ch}}{\partial t} = \Sigma\frac{\chi_i M_{H_2O}\omega_i\rho_s(1-\varphi)}{M_i}\frac{\partial\xi_i}{\partial t}. \tag{B10}$$

Here χ_i and M_i are water-containing index and molar mass of the reactant (i). As aforementioned, a phase transition can be considered as a process that a certain mass/volume of liquid water is replaced by the vapor water (or in the reverse direction). Neglecting variation in liquid phase density (ρ_l), as is appropriate for the (nearly) isothermal conditions in an iteration step, the mass change rate can be accordingly expressed as follows:

$$\partial m_{lv}/\partial t = \varphi\rho_l(\partial S_l/\partial t). \tag{B11}$$

Substituting equations (B7)–(B11) into (B1), divided by their respective phase densities yields

$$\varphi S_l\left(\beta_l + \beta_p\right)\frac{\partial p}{\partial t} - \varphi S_l(\alpha_l - \alpha_s)\frac{\partial T}{\partial t} + S_l\left(\frac{\partial \varphi_{ch}}{\partial t} + \frac{\partial \varphi_d}{\partial t}\right) + \varphi\frac{\partial S_l}{\partial t} = \frac{\partial}{\partial x}\left(\frac{k_{rl}k\partial p}{\eta_l\ \partial x}\right) + \varphi\frac{\partial S_l}{\partial t} + \frac{1}{\rho_l}\frac{\partial m_{ch}}{\partial t}$$

$$\varphi S_v\left(\beta_v + \beta_p\right)\frac{\partial p}{\partial t} - \varphi S_v(\alpha_v - \alpha_s)\frac{\partial T}{\partial t} + S_v\left(\frac{\partial \varphi_{ch}}{\partial t} + \frac{\partial \varphi_d}{\partial t}\right) + \varphi\frac{\partial S_v}{\partial t} = \frac{\partial}{\partial x}\left(\frac{k_{rv}k\partial p}{\eta_v\ \partial x}\right) - \frac{\rho_l}{\rho_v}\frac{\partial S_l}{\partial t}. \qquad (B12)$$

Summing up the two equations in (B12) and with the relation that $S_v + S_l = 1$ gives the mass conservation equation for a two-phase mixture model:

$$\varphi\left(\beta_f + \beta_p\right)\frac{\partial p}{\partial t} - \varphi(\alpha_f - \alpha_s)\frac{\partial T}{\partial t} + \left(\frac{\partial \varphi_{ch}}{\partial t} + \frac{\partial \varphi_d}{\partial t}\right) = \frac{\partial}{\partial x}\left(\frac{k}{\eta_f}\frac{\partial p}{\partial x}\right) + \varphi\left(\frac{\rho_l}{\rho_v} - 1\right)\frac{\partial S_v}{\partial t} + \frac{1}{\rho_l}\frac{\partial m_{ch}}{\partial t}. \qquad (B13)$$

In this equation, the properties with subscript f (i.e., α_f, β_f, and η_f) stand for the properties of the two-phase mixture [*Wang and Beckermann*, 1993], which are accordingly defined as follows:

$$\beta_f = S_v\beta_v + S_l\beta_l$$
$$\alpha_f = S_v\alpha_v + S_l\alpha_l \qquad (B14)$$
$$\eta_f = 1/(k_{rl}/\eta_l + k_{rv}/\eta_v).$$

Note that the dynamic viscosity (η_f) expressed in (B14) is less than perfect. This is because the momentum equations given in (B8) do not include the partial derivatives of densities, resulting in a superficial mixture velocity that is related to the intrinsic single-phase velocities by the phase volume fractions. Referring to the mass flux as in (B1), $\rho_f\mathbf{u_f} = \rho_l u_l + \rho_v u_v$, the mixture velocity is virtually a mass-weighted average of the single-phase velocities. By virtue of this, the momentum equations for liquid and vapor phases are then multiplied by their respective densities, with the sum giving the mixture velocity, that is, $\rho_f\mathbf{u_f} = -k\nabla p_l \cdot (k_{rl}/v_l) - k\nabla p_v \cdot (k_{rv}/v_v) = -k\nabla p/v_f$, where $v_f = 1/(k_{rl}/v_l + k_{rv}/v_v)$ is defined as the *mean* kinematic viscosity of a two-phase mixture [*Chavent*, 1976]. According to the definition that $\eta = \rho v$, the dynamic viscosity of a two-phase mixture is more elaborately expressed as follows:

$$\eta_f = \rho_f v_f = \frac{S_l\rho_l + S_v\rho_v}{k_{rl}/v_l + k_{rv}/v_v}. \qquad (B15)$$

A rigorous derivation of (B15), with a bit more algebraic manipulations, has been given in details by *Wang and Beckermann* [1993]. In our study, the relative permeabilities are simply chosen as linear function, that is,

$$k_{rl} = S_l \text{ and } k_{rv} = S_v \qquad (B16)$$

for the liquid and gas phases, respectively. For incohesive fault rocks, the mineral compressibility is relatively small compared to that of the pores, leading to the specific storage being expressed as $S_s \approx \varphi(\beta_f + \beta_p)$ [*Rice*, 2006]. Further, using the relations for chemical reactions ($\partial\varphi_{ch}/\partial t$ in equation (B6) and $\partial m_{ch}/\partial t$ in equation (B10)), equation (B13) can be simplified into

$$S_s\frac{dp}{dt} = \frac{\partial}{\partial x}\left(\frac{k}{\eta_f}\frac{\partial p}{\partial x}\right) + \Omega_T + \Omega_{ch} + \Omega_{lv} - \frac{d\varphi_d}{dt}. \qquad (B17)$$

In this final equation, $\Omega_T = \varphi(\alpha_f - \alpha_s)\frac{dT}{dt}$, $\Omega_{ch} = \sum\omega_i(1-\varphi)\Pi_i\frac{d\xi_i}{dt}$, and $\Omega_{lv} = \varphi\left(\frac{\rho_l}{\rho_v} - 1\right)\frac{dS_v}{dt}$ express the fluid volume expansion/generation rates per unit volume rock caused by thermal pressurization, chemical reactions, and water vaporization, respectively, where the term $\Pi_i = \frac{\chi_i M_{H_2O}}{M_i}\frac{\rho_s}{\rho_l} - \Delta V_i$ is the specific expelled water for chemical reaction (i). Constitutive relationships for the two-phase fluid properties in (B17) are given in (B14)–(B16) (summarized in Table 1).
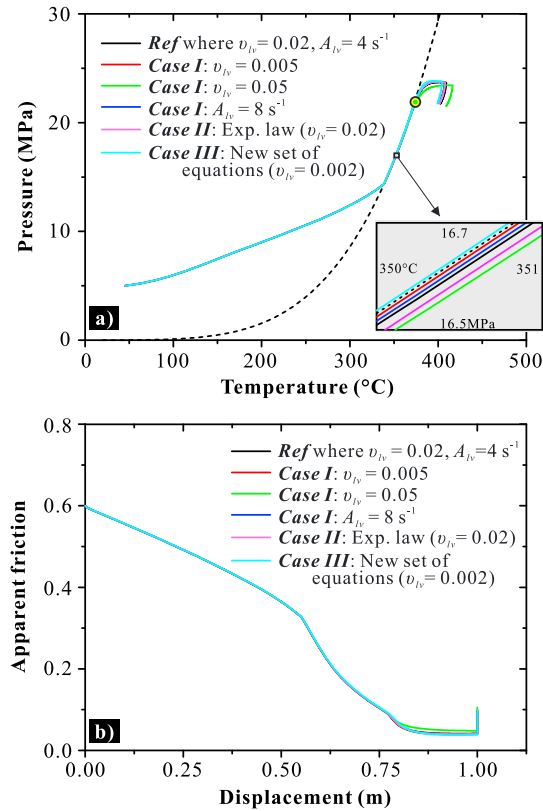
Figure C1. Validation of the method that we proposed in this study to model a phase transition. Comparison of the modeling results of (a) the PT state evolution of pore fluid at the PSZ center and (b) the evolution of apparent friction with displacement, from three different cases (*Cases I–III*). In *Case I*, we use the same kinetic function as in the main paper (equations (C1a) and (C1b)), but we vary the v_{lv} and A_{lv} values. In *Case II*, a kinetic function in an exponential form (equations (C2a) and (C2b)) is used to describe the phase transition (with the same v_{lv} value). In *Case III*, a new system of governing equations is used for the simulation (see a new set of equations in (C9a) and (C9b), in which a kinetic function is not needed). See details about the three cases in the text of Appendix C.

Appendix C: Validation of the Method Proposed to Model a Phase Transition

In the main text, tangent functions are used to describe the kinetics of the phase transition. They are

$$\kappa_{l-v}(v) = A_{lv} \tan\left(\frac{\pi}{2}\frac{v}{v_{lv}}\right)(v > 0) \tag{C1a}$$

and

$$\kappa_{v-l}(v) = A_{lv} \tan\left(\frac{\pi}{2}\frac{v}{v_{lv}}\right)(v < 0) \tag{C1b}$$

for the vaporization and condensation processes, respectively (see also equations (13a) and (13b)). To further elaborate the validity of this method, additional models have been performed as follows:

Case I. In the main body (Figures 6–15), we use v_{lv} of 0.02 and A_{lv} of 4 s^{-1}. The results show that the PT state of the pore water evolves along the liquid-vapor transition curve (Figure C1a). In order to test the sensitivity to these parameters, different values of v_{lv} (0.005–0.05) and A_{lv} (1–8 s^{-1}) are used.

Case II. As an alternative, exponential functions are used to describe the phase transition rates. They are

$$\kappa_{l-v}(v) = A_{lv} \exp\left(-\frac{v_{lv}}{v}\right)(v > 0) \tag{C2a}$$

and

$$\kappa_{v-l}(v) = -A_{lv} \exp\left(\frac{v_{lv}}{v}\right)(v < 0) \tag{C2b}$$

for vaporization and condensation, respectively. Likewise, the v_{lv} value in these functions specifies the "width" of the two-phase coexistent zone, and we use the same v_{lv} value of 0.02. The A_{lv} value indicates the maximum "transition rate" and a relatively large value of 8 s^{-1} is used.

Case III. Actually, it is not always necessary to describe the phase transition kinetics (dS_v/dt) in explicit functions. For a phase transition between two phases of matter of a single constituent, the PT conditions should conform to the Clapeyron relation, that is,

$$\Gamma = dp/dT. \tag{C3}$$

This equation suggests that the evolution of pressure and temperature are virtually interdependent during a phase transition. Reformulating (C3) into a form of a differential equation, yields

$$\frac{\partial T}{\partial t} = \frac{\partial p}{\partial t}\Gamma^{-1} \tag{C4}$$

On one hand, as given in equations (4) and (8), Q_{lv} and Ω_{lv} are both functions of the phase transition kinetics (dS_v/d_t). Coupling Ω_{lv} and Q_{lv}, and eliminating the term dS_v/dt, gives

$$\Omega_{lv} = \left(\frac{1}{\rho_v} - \frac{1}{\rho_l}\right)\frac{M_{H_2O}}{\Delta H_{lv}}Q_{lv}. \tag{C5}$$

On the other hand, the energy conservation equation can be reformulated into

$$Q_{lv} = \rho_b c_b \frac{\partial T}{\partial t} - \frac{\partial}{\partial x}\left(K_b \frac{\partial T}{\partial x}\right) - Q_{fr} - Q_{ch}. \tag{C6}$$

Combining (C5) and (C6), we have

$$\Omega_{lv} = \left(\frac{1}{\rho_v} - \frac{1}{\rho_l}\right)\frac{M_{H_2O}}{\Delta H_{lv}} \cdot \left[\rho_b c_b \frac{\partial T}{\partial t} - \frac{\partial}{\partial x}\left(K_b \frac{\partial T}{\partial x}\right) - Q_{fr} - Q_{ch}\right]. \tag{C7}$$

Now an enclosed assembly of equations (5), (9), (C4), and (C7) composes the new set of equations describing the coseismic thermochemical pressurization, with the presence of water phase transition:

$$S_s\frac{\partial p}{\partial t} = \frac{\partial}{\partial x}\left(\frac{k}{\eta_f}\frac{\partial p}{\partial x}\right) + \Omega_T + \Omega_{ch} + \Omega_{lv} - \frac{d\varphi_d}{dt}$$
$$\frac{\partial T}{\partial t} = \frac{\partial p}{\partial t}\Gamma^{-1}$$
$$\frac{\partial \xi_i}{\partial t} = f_i(\xi_i)\kappa_i(T) \tag{C8}$$
$$\Omega_{lv} = \left(\frac{1}{\rho_v} - \frac{1}{\rho_l}\right)\frac{M_{H_2O}}{\Delta H_{lv}} \cdot \left[\rho_b c_b \frac{\partial T}{\partial t} - \frac{\partial}{\partial x}\left(K_b \frac{\partial T}{\partial x}\right) - Q_{fr} - Q_{ch}\right].$$

As in the main text, the occurrence of a phase transition can be specified by the relation that $|v| < v_{lv}$ (Figure 3). Here we define it as a Boolean variable $[B] = (|v| < v_{lv})$, and its negation $[!B]$ denotes the absence of any phase transition. Using this variable, the governing equations with or without a phase transition can be written into a uniform form, consisting of three differential equations:

$$S_s\frac{\partial p}{\partial t} = \frac{\partial}{\partial x}\left(\frac{k}{\eta_f}\frac{\partial p}{\partial x}\right) + \Omega_T + \Omega_{ch} + \Omega_{lv} - \frac{d\varphi_d}{dt}$$
$$\rho_b c_b\frac{\partial T}{\partial t} = [B]\cdot\rho_b c_b\frac{\partial p}{\partial t}\Gamma^{-1} + [!B]\cdot\left[\frac{\partial}{\partial x}\left(K_b\frac{\partial T}{\partial x}\right) + Q_{fr} + Q_{ch}\right] \tag{C9a}$$
$$\frac{\partial \xi_i}{\partial t} = f_i(\xi_i)\kappa_i(T)$$

plus an ordinary equation

$$\Omega_{lv} = [B]\cdot\left(\frac{1}{\rho_v} - \frac{1}{\rho_l}\right)\frac{M_{H_2O}}{\Delta H_{lv}} \cdot \left[\rho_b c_b \frac{\partial T}{\partial t} - \frac{\partial}{\partial x}\left(K_b \frac{\partial T}{\partial x}\right) - Q_{fr} - Q_{ch}\right]. \tag{C9b}$$

The latter only arises in the presence of a phase transition ($[B] = 1$). When $[B] = 0$, (C9b) does not exist and the equation set reduces to that for thermochemical pressurization (cf. equation (15)). Since we avoid using the

kinetic equation, the number of differential equations in (C9a) and (C9b) is one less than that in the equation set (14). Despite these advantages, the main problem to apply equation set (C9a) and (C9b) lies on the computation difficulty. To judge if a phase transition is occurring or not at each individual node of the model ([*B*] = 0 or 1), the time step needs to be very small; otherwise, it will give rise to unstable behavior with repeated back-and-forth phase transitions that limit convergence rate. When modeling the reference case with (C9a) and (C9b), it entails a time step to be 0.0001 s and the option of "adaptive time step" (as embedded in COMSOL) needs to be chosen. It is very time consuming (it takes more than 2 h to implement a single case of modeling), and the practical time step turns out to be as small as 0.00002 s during the iteration.

Except otherwise stated, all the settings for the three models (*Cases I–III*) are the same as the reference case (Table 2). As given in Figure C1, all the three cases produce almost the same results, irrespective of the kinetic functions (i.e., equations (C1a) and (C1b) versus (C2a) and (C2b)) or the equations used (i.e., equation sets (14) versus (C9a) and (C9b)). The broad consistency confirms the method we propose in the present study to model a phase transition. Furthermore, since the kinetic function is avoided in *Case III*, the results can be taken as some sort of "true solution." The PT state of pore water in this case indeed evolves along the SVC (see the exaggerated graph in Figure C1a). A comparison of the results from *Case I*, in which we use different v_{lv} and A_{lv} values, indicates that the model is not sensitive to the A_{lv} value but may suffer from uncertainty when large v_{lv} value is used.

Appendix D: Representative Results Showing the Evolution of Fluid and Transport Properties

When vaporization occurs, the fluid flow becomes a two-phase system. Due to the discontinuity feature between liquid and vapor phases, the fluid properties can undergo large variations. Figure D1 gives the representative results, showing the evolution of density, thermal expansivity, compressibility, and dynamic viscosity of the pore fluid in the center of the PSZ gouge. As the pore fluid vaporizes, the fluid pressurization effect
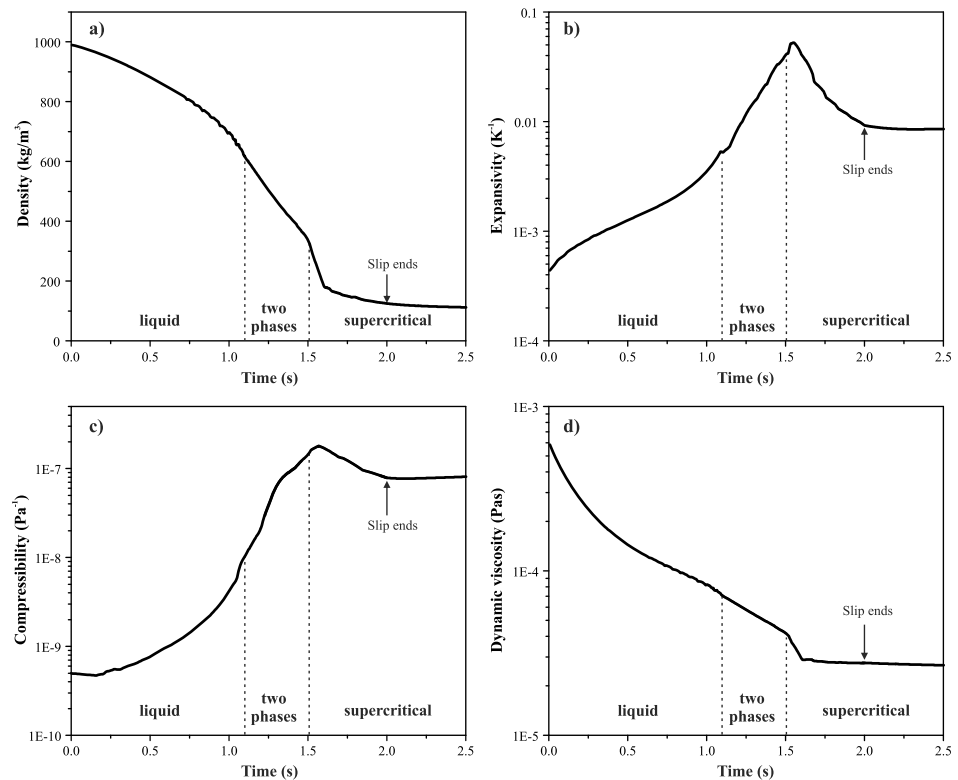
Figure D1. Evolution of fluid properties (density, expansivity, compressibility, and dynamic viscosity) at the center of the principal slip zone in the reference case of modeling (as Figure 6).
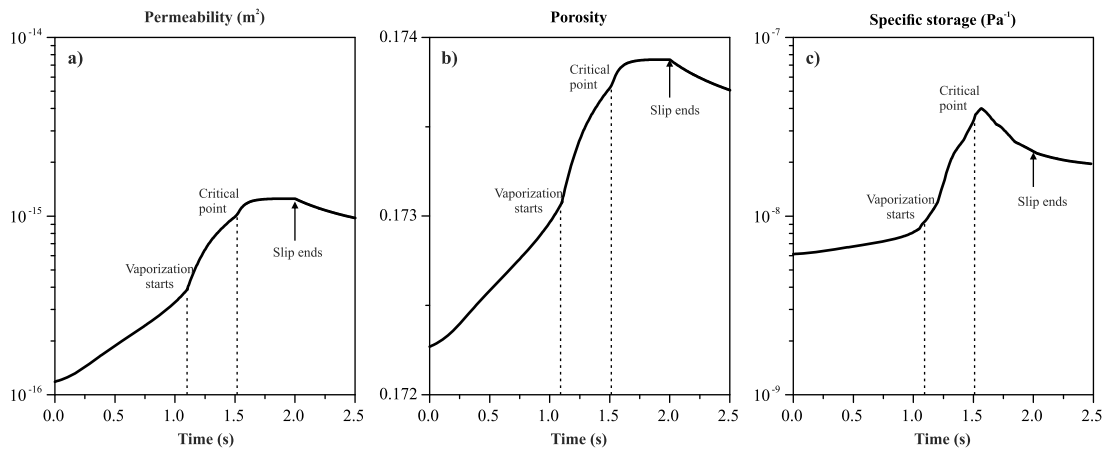
Figure D2. Evolution of transport properties ((a) permeability, (b) porosity, and (c) specific storage) of the principal slip zone in the reference case of modeling.

will reduce the effective normal stress acting on the fault plane, therefore increasing the permeability and porosity (Figure D2). The specific storage will also increase, but, as determined via $S_s = \beta_b + \varphi\beta_f - (1 + \varphi)\beta_s$ [*Brace et al.*, 1968], is affected by the fluid compressibility as well.

Notation

Parameters	Symbol	Units
Fault zone configuration parameters		
Distance normal to a fault plane	x	m
Depth	z	km
Time	t	s
Temperature	T	K
Ambient temperature	T_a	K
Thermal gradient	dT/dz	°C km^{-1}
Hydrostatic/lithostatic pressure coefficient	λ	
Normal stress acting on fault plane	σ_n	MPa
Confining pressure = σ_n	P_c	MPa
Pore pressure	p	MPa
Terzaghi effective pressure	P_e	MPa
Mean pore pressure in the shear band	$\bar{p}$	MPa
Ambient pore pressure	p_a	MPa
Initial pore pressure in the shear band	p_{PSZ}	MPa
Slip velocity	V	ms^{-1}
Displacement	L	m
Slip band thickness	w	m
Fluid and solid properties		
Mass[a]	m	kg
Enthalpy[a]	h	J kg^{-1}
Specific heat[a]	c	J kg^{-1} K^{-1}
Thermal conductivity[a]	K	Wm^{-1} K^{-1}
Density[a]	ρ	kgm^{-3}
Dynamic viscosity[a]	η	Pa s
Kinematic viscosity[a]	v	m^2 s^{-1}
Thermal expansivity[a]	α	K^{-1}
Compressibility[a]	β	Pa^{-1}
Reaction-related parameters		
Concentration of reactant (*i*)	ξ_i	
Activation energy for reaction (*i*)	E_i	J mol^{-1}
Enthalpy change of reaction (*i*)	ΔH_i	J mol^{-1}
Reaction rate constant for reaction (*i*)	A_i	s^{-1}
Gas constant	R	J K^{-1} mol^{-1}

Wight content of reactant (i)	ω_i	[0,1]
Molar mass of reactant (i)	M_i	kg mol^{-1}
Molar mass of water	M_{H2O}	kg mol^{-1}
Water-containing index of reactant (i)	χ_i	
Specific solid volume shrinkage by reaction (i)	ΔV_i	m^3 m^{-3}
Specific expelled water for reaction (i)	Π_i	m^3 m^{-3}
Heat sink by chemical reaction(s)	Q_{ch}	J m^{-3} s^{-1}
Fluid volume generation rate by reaction(s)	Ω_{ch}	m^3 m^{-3} s^{-1}
Phase change-related parameters		
Vapor saturation	S_v	
Liquid saturation	S_l	
Boiling temperature for a phase transition	T_{SVC}	K
Pressure of saturated vapor	p_{SVC}	MPa
State variable defined to specify the PT state of water	υ	
Threshold state value for inhibiting oversaturation	υ_{lv}	
Vaporization/condensation rate constant	A_{lv}	s^{-1}
Vaporization rate	$\kappa_{l\text{-}v}$	s^{-1}
Condensation rate	$\kappa_{v\text{-}l}$	s^{-1}
Boolean variable for the occurrence of a phase transition	$[B]$	0 or 1
Specific volume change of a phase transition	ΔV_{lv}	m^3 kg^{-1}
Enthalpy change of a phase transition	Δh_{lv}	J kg^{-1}
Enthalpy change of a phase transition	ΔH_{lv}	J mol^{-1}
Solid enthalpy at zero-K (a reference value)	h_{s0}	J kg^{-1}
Heat sink by a phase transition	Q_{lv}	J m^{-3} s^{-1}
Fluid volume expansion rate by a phase transition	Ω_{lv}	m^3 m^{-3} s^{-1}
Clausius-Clapeyron slope of a phase transition	Γ	Pa/K
Hydraulic parameters		
Intrinsic permeability of fault rocks	k	m^2
Relative permeability of liquid water	k_{rl}	
Relative permeability of vapor water	k_{rv}	
Effective porosity of fault rocks	φ	
Pressure-sensitivity of transport properties	ε	Pa^{-1}
Specific storage of fault rocks	S_s	Pa^{-1}
Darcy flow velocity[a]	$\mathbf{u}$	ms^{-1}
Inelastic porosity change	$\Delta\varphi_p$	
Dilatancy-induced porosity change	$\Delta\varphi_d$	
Reaction-induced porosity change (related to ΔV_i)	$\Delta\varphi_{ch}$	
Thermal diffusivity length	L_t	m
Hydraulic diffusivity length	L_h	m
Friction parameters		
Dynamic friction coefficient	μ_d	
Peak friction coefficient	μ_p	
Steady-state friction coefficient	μ_{ss}	
Characteristic slip-weakening distance	d_c	m
Apparent friction coefficient ($\mu_a = \tau/(P_c - p_{PSZ})$)	μ_a	
Frictional heat generation rate	Q_{fr}	J m^{-3} s^{-1}
Fluid volume expansion rate by frictional heating	Ω_T	m^3 m^{-3} s^{-1}
Total frictional work	W_f	M J/m^2
Critical W_f for the onset of vaporization	W_{cr}	M J/m^2
Subscript		
Bulk sample	b	
Solid grains	s	
Pore fluid in general	f	
Vapor phase fluid	v	
Liquid phase fluid	l	
Chemical reaction	ch	
Liquid-to-vapor (vaporization)	$l-v$	
Vapor-to-liquid (condensation)	$v\text{-}l$	
Phase transition (without a specific sense)	lv	
On/along the saturated vapor curve	SVC	

[a]The parameters with superscript "a" have different subscripts, b, s, f, l, and v, denoting quantities for the bulk sample, the solid grains, the pore fluid in general, the liquid, and vapor phases, respectively. At supercritical state, $X_f = X_l = X_v$, where X indicates a fluid parameter.

References

Andrews, D. J. (2002), A fault constitutive relation accounting for thermal pressurization of pore fluid, *J. Geophys. Res.*, *107*(B12), 2363, doi:10.1029/2002JB001942.

Anderson, D. L. (1985), Calculation of slide velocities, in *The Vaiont Slide: A Geotechnical Analysis Based on New Geologic Observations of the Failure Surface*, Tech. Rep. GL-85-5, edited by A. J. Hendron and F. D. Patton, pp. 87–90, U.S. Army Corp. of Eng. Waterw. Exper. Stn., Washington, D. C.

Bayer, G. (1973), Thermal expansion anisotropy of oxide compounds, *Proc. Br. Ceram. Soc.*, *22*, 39–53.

Beeler, N. M., T. E. Tullis, and D. L. Goldsby (2008), Constitutive relationships and physical basis of fault strength due to flash heating, *J. Geophys. Res.*, *113*, B01401, doi:10.1029/2007JB004988.

Birch, F. (1966), Compressibility: Elastic constants, in *Handbook of Physical Constants*, edited by D. P. Clark, Jr., *Geol. Soc. Am. Mem.*, 97, 97–174.

Bizzarri, A., and M. Cocco (2006), A thermal pressurization model for the spontaneous dynamic rupture propagation on a three-dimensional fault: 1. Methodological approach, *J. Geophys. Res.*, *111*, B05303, doi:10.1029/2005JB003862.

Brace, W. F., J. B. Walsh, and W. T. Frangos (1968), Permeability of granite under high pressure, *J. Geophys. Res.*, *73*, 2225–2236, doi:10.1029/JB073i006p02225.

Bradbury, K. K., J. P. Evans, J. S. Chester, F. M. Chester, and D. L. Kirschner (2011), Lithology and internal structure of the San Andreas fault at depth based on characterization of phase 3 whole-rock core in the San Andreas Fault Observatory at Depth (SAFOD) borehole, *Earth Planet. Sci. Lett.*, *310*, 131–144.

Boutareaud, S., A. M. Boullier, M. Andreani, D. G. Calugaru, P. Beck, S.-R. Song, and T. Shimamoto (2010), Clay-clast aggregates in gouges: New textural evidence for seismic fault sliding, *J. Geophys. Res.*, *115*, B02408, doi:10.1029/2007GL032554.

Brantut, N., A. Schubnel, J. Corvisier, and J. Sarout (2010), Thermochemical pressurization of faults during coseismic slip, *J. Geophys. Res.*, *115*, B05314, doi:10.1029/2009JB006533.

Brantut, N., J. Sulem, and A. Schubnel (2011a), Effect of dehydration reactions on earthquake nucleation: Stable sliding, slow transients, and unstable slip, *J. Geophys. Res.*, *116*, B05304, doi:10.1029/2010JB007876.

Brantut, N., R. Han, T. Shimamoto, N. Findling, and A. Schubnel (2011b), Fast slip with inhibited temperature rise due to mineral dehydration: Evidence from experiments on gypsum, *Geology*, *39*, 59–62.

Brantut, N., F. X. Passelègue, D. Deldicque, J. N. Rouzaud, and A. Schubnel (2016), Dynamic weakening and amorphization in serpentinite during laboratory earthquakes, *Geology*, *44*(8), 607–610.

Chavent, G. (1976), A new formulation of diphasic incompressible flows in porous media, in *Lecture Notes in Mathematics*, vol. 503, pp. 258–270, Springer, New York.

Chen, J., X. Yang, J. Dang, C. He, Y. Zhou, and S. Ma (2011), Internal structure and permeability of Wenchuan earthquake fault [in Chinese with an English abstract], *Chin. J. Geophys.*, *54*(7), 1805–1916.

Chen, J., X. Yang, Q. Duan, T. Shimamoto, and C. J. Spiers (2013), Importance of thermochemical pressurization in the dynamic weakening of the Longmenshan fault during the 2008 Wenchuan earthquake: Inferences from experiments and modeling, *J. Geophys. Res. Solid Earth*, *118*, 4145–4169, doi:10.1002/jgrb.50260.

Chen, J., X. Yang, S. Ma, T. Yang, and A. Niemeijer (2016), Hydraulic properties of samples retrieved from the Wenchuan earthquake fault scientific drilling project hole-1 (WFSD-1) and the surface rupture zone: Implications for coseismic slip weakening and fault healing, *Geochem. Geophys. Geosyst.*, *17*, 2717–2744, doi:10.1002/2016GC006376.

Chen, J., A. Niemeijer, L. Yao, and S. Ma (2017), Water vaporization promotes coseismic fluid pressurization and buffers temperature rise, *Geophys. Res. Lett.*, *44*, 2177–2185, doi:10.1002/2016GL071932.

Chester, F. M., and J. S. Chester (1998), Ultracataclasite structure and friction processes of the Punchbowl fault, San Andreas system, California, *Tectonophysics*, *295*, 199–221.

Dagan, G. (1988), Time-dependent macrodispersion for solute transport in anisotropic heterogeneous aquifers, *Water Resour. Res.*, *24*(9), 1491–1500, doi:10.1029/WR024i009p01491.

De Paola, N., T. Hirose, and T. Mitchell (2011), Fault lubrication and earthquake propagation in thermally unstable rocks, *Geology*, *39*(1), 35–38.

Di Toro, G., D. Goldsby, and T. E. Tullis (2004), Friction falls towards zero in quartz rock as slip velocity approaches seismic rates, *Nature*, *427*, 436–439.

Di Toro, G., G. Pennacchioni, and G. Teza (2005), Can pseudotachylytes be used to infer earthquake source parameters? An example of limitations in the study of exhumed faults, *Tectonophysics*, *402*, 3–20.

Di Toro, G., R. Han, T. Hirose, N. De Paola, S. Nielsen, K. Mizoguchi, F. Ferri, M. Cocco, and T. Shimamoto (2011), Fault lubrication during earthquakes, *Nature*, *471*, 493–499.

Duan, Q., X. Yang, and J. Chen (2016), Internal structure and permeability of the Yingxiu-Beichuan fault activated during the 2008 Wenchuan earthquake, China, *AOGS Conference*, Abstract SE10-A029.

Faulkner, D. R., T. M. Mitchell, J. Behnen, T. Hirose, and T. Shimamoto (2011), Stuck in the mud? Earthquake nucleation and propagation through accretionary forearcs, *Geophys. Res. Lett.*, *38*, L18303, doi:10.1029/2011GL048552.

Ferri, F., G. Di Toro, T. Hirose, and T. Shimamoto (2010), Evidence of thermal pressurization in high-velocity friction experiments on smectite rich gouges, *Terra Nova*, *22*, 347–353.

Ferri, F., G. Di Toro, T. Hirose, R. Han, H. Noda, T. Shimamoto, M. Quaresimin, and N. de Rossi (2011), Low- to high-velocity frictional properties of the clay-rich gouges from the slipping zone of the 1963 Vaiont slide, northern Italy, *J. Geophys. Res.*, *116*, B09208, doi:10.1029/2011JB008338.

Garagash, D. I. (2012), Seismic and aseismic slip pulses driven by thermal pressurization of pore fluid, *J. Geophys. Res.*, *117*, B04314, doi:10.1029/2011JB008889.

Garagash, D. I., and J. W. Rudnicki (2003), Shear heating of a fluid saturated slip weakening dilatant fault zone: 1. Limiting regimes, *J. Geophys. Res.*, *108*(B2), 2121, doi:10.1029/2001JB001653.

Goldsby, D. L., and T. E. Tullis (2002), Low frictional strength of quartz rocks at subseismic slip rates, *Geophys. Res. Lett.*, *29*(17), 1844, doi:10.1029/2002GL015240.

Goldsby, D. L., and T. E. Tullis (2011), Flash heating leads to low frictional strength of crustal rocks at earthquake slip rates, *Science*, *334*, 216–218.

Habib, P. (1975), Production of gaseous pore pressure during rock slides, *Rock Mech.*, *7*, 193–197.

Hamada, Y., T. Hirono, M. Ikehara, W. Soh, and S. Song (2009), Estimated dynamic shear stress and frictional heat during the 1999 Taiwan Chi-Chi earthquake: A chemical kinetics approach with isothermal heating experiments, *Tectonophysics*, *469*, 73–84.

Han, R., T. Shimamoto, T. Hirose, J. Ree, and J. Ando (2007), Ultralow friction of carbonate faults caused by thermal decomposition, *Science*, *316*, 878–881.

Han, R., T. Hirose, and T. Shimamoto (2010), Strong velocity weakening and powder lubrication of simulated carbonate faults at seismic slip rates, *J. Geophys. Res.*, *115*, B03412, doi:10.1029/2008JB006136.

Hemingway, B. S. (1987), Quartz: Heat capacities from 340 to 1000 K and revised values for the thermodynamic properties, *Am. Mineral.*, *72*, 273–279.

Hirono, T., et al. (2006), High magnetic susceptibility of fault gouge within Taiwan Chelungpu fault: Nondestructive continuous measurements of physical and chemical properties in fault rocks recovered from hole B, TCDP, *Geophys. Res. Lett.*, *33*, L15303, doi:10.1029/2006GL026133.

Hirono, T., Y. Maekawa, and H. Yabuta (2015), Investigation of the records of earthquake slip in carbonaceous materials from the Taiwan Chelungpu fault by means of infrared and Raman spectroscopies, *Geochem. Geophys. Geosyst.*, *16*, 1233–1253, doi:10.1002/2014GC005622.

Hirose, T., and M. Bystricky (2007), Extreme dynamic weakening of faults during dehydration by coseismic shear heating, *Geophys. Res. Lett.*, *34*, L14311, doi:10.1029/2007GL030049.

Hirose, T., and T. Shimamoto (2005), Growth of molten zone as a mechanism of slip weakening of simulated faults in gabbro during frictional melting, *J. Geophys. Res.*, *110*, B05202, doi:10.1029/2004JB003207.

Huang, S.-W., J.-S. Jean, and J.-C. Hu (2003), Huge rock eruption caused by the 1999 Chi-Chi earthquake in Taiwan, *Geophys. Res. Lett.*, *30*(16), 1858, doi:10.1029/2004JB003207.

Huang, W. L., W. A. Bassett, and T. C. Wu (1994), Dehydration and hydration of montmorillonite at elevated temperatures and pressures monitored using synchrotron radiation, *Am. Mineral.*, *79*, 683–691.

Ikehara, M., et al. (2007), Low total and inorganic carbon contents within the Chelungpu fault system, *Geochem. J.*, *41*, 391–396.

Ishikawa, T., et al. (2008), Coseismic fluid-rock interactions at high temperatures in the Chelungpu fault, *Nat. Geosci.*, *1*, 679–683.

Kameda, J., M. Shimizu, K. Ujiie, T. Hirose, M. Ikari, J. Mori, K. Oohashi, and G. Kimura (2015), Pelagic smectite as an important factor in tsunamigenic slip along the Japan Trench, *Geology*, doi:10.1130/G35948.1.

Kitajima, H., J. S. Chester, F. M. Chester, and T. Shimamoto (2010), High-speed friction of disaggregated ultracataclasite in rotary shear: Characterization of frictional heating, mechanical behavior, and microstructure evolution, *J. Geophys. Res.*, *115*, B08408, doi:10.1029/2009JB007038.

Kitajima, H., F. M. Chester, and J. S. Chester (2011), Dynamic weakening of gouge layers in high-speed shear experiments: Assessment of temperature-dependent friction, thermal pressurization, and flash heating, *J. Geophys. Res.*, *116*, B08309, doi:10.1029/2010JB007879.

Kuo, L. W., S. R. Song, L. Huang, E. C. Yeh, and H. F. Chen (2011), Temperature estimates of coseismic heating in clay-rich fault gouges, the Chelungpu fault zone, Taiwan, *Tectonophysics*, *502*, 315–327.

Lachenbruch, A. H. (1980), Frictional heating, fluid pressure, and the resistance to fault motion, *J. Geophys. Res.*, *85*, 6097–6112, doi:10.1029/JB085iB11p06097.

Lee, S. L., and R. Y. Tzong (1991), An enthalpy formulation for phase change problems with a large thermal diffusivity jump across the interface, *Int. J. Heat Mass Transfer*, *34*(6), 1491–1502.

Li, H., et al. (2015), Long-term temperature records following the M_w 7.9 Wenchuan (China) earthquake consistent with low friction, *Geology*, *43*(2), 163–166.

Lockner, D. A., M. J. S. Johnston, and J. D. Byerlee (1983), A mechanism to explain the generation of earthquake lights, *Nature*, *302*, 28–33.

Ma, K. F., et al. (2006), Slip zone and energetics of a large earthquake from the Taiwan Chelungpu-fault drilling project, *Nature*, *444*, 473–476.

Maekawa, Y., T. Hirono, H. Yabuta, H. Mukoyoshi, M. Kitamura, M. Ikehara, W. Tanikawa, and T. Ishikawa (2014), Estimation of slip parameters associated with frictional heating during the 1999 Taiwan Chi-Chi earthquake by vitrinite reflectance geothermometry, *Earth Planets Space*, *66*, 28.

Marone, C., C. B. Raleigh, and C. H. Scholz (1990), Frictional behavior and constitutive modeling of simulated fault gouge, *J. Geophys. Res.*, *95*, 7007–7025, doi:10.1029/JB095iB05p07007.

Mase, C. W., and L. Smith (1987), Effects of frictional heating on the thermal, hydrologic, and mechanical response of a fault, *J. Geophys. Res.*, *92*, 6249–6272, doi:10.1029/JB092iB07p06249.

Mishima, T., T. Hirono, W. Soh, and S. Song (2006), Thermal history estimation of the Taiwan Chelungpu fault using rock-magnetic methods, *Geophys. Res. Lett.*, *33*, L23311, doi:10.1029/2006GL028088.

Mizoguchi, K., T. Hirose, T. Shimamoto, and E. Fukuyama (2007a), Reconstruction of seismic faulting by high-velocity friction experiments: An example of the 1995 Kobe earthquake, *Geophys. Res. Lett.*, *34*, L01308, doi:10.1029/2006GL027931.

Mizoguchi, K., M. Takahashi, K. Masuda, and E. Fukuyama (2007b), Fault strength drop due to phase transitions in the pore fluid, *Geophys. Res. Lett.*, *34*, L09313, doi:10.1029/2007GL029345.

Mizoguchi, K., T. Hirose, T. Shimamoto, and E. Fukuyama (2008), Internal structure and permeability of the Nojima fault, southwest Japan, *J. Struct. Geol.*, *30*, 513–524.

Mizoguchi, K., T. Hirose, T. Shimamoto, and E. Fukuyama (2009), High velocity frictional behavior and microstructure evolution of fault gouge obtained from Nojima fault, southwest Japan, *Tectonophysics*, *471*, 285–296.

Moore, D. E., and M. J. Rymer (2007), Talc-bearing serpentinite and the creeping section of the San Andreas Fault, *Nature*, *448*, 795–797.

Morrow, C. A., A. Lockner, and S. Hickman (2014), Deep permeability of the San Andreas Fault from San Andreas Fault Observatory at Depth (SAFOD) core samples, *J. Struct. Geol.*, *64*, 99–114.

Muhieddine, M., E. Canot, and R. March (2009), Various approaches for solving problems in heat conduction with phase change, *Int. J. Finite*, *6*, 1–20.

Niemeijer, A., G. Di Toro, S. A. F. Smith, A. W. Griffith, A. Bistacchi, and S. Nielsen (2012), Inferring earthquake physics and chemistry using an integrated field and laboratory approach, *J. Struct. Geol.*, *39*, 2–36.

Noda, H., and N. Lapusta (2010), Three-dimensional earthquake sequence simulations with evolving temperature and pore pressure due to shear heating: Effect of heterogeneous hydraulic diffusivity, *J. Geophys. Res.*, *115*, B12314, doi:10.1029/2010JB007780.

Noda, H., and L. Lapusta (2013), Stable creeping fault segments can become destructive as a result of dynamic weakening, *Nature*, *518*, doi:10.1038/nature11703.

Noda, H., and T. Shimamoto (2005), Thermal pressurization and slip weakening distance of a fault: An example of Hanaore fault, southwest Japan, *Bull. Seismol. Soc. Am.*, *95*(4), 1224–1233.

Noyan, H., M. Önal, and Y. Sarikaya (2008), Thermal deformation thermodynamics of a smectite mineral, *J. Therm. Anal. Calorim.*, *91*, 299–303.

Otsuki, K., T. Hirono, M. Omori, M. Sagaguchi, W. Tanigawa, W. Lin, W. Soh, and S. Song (2009), Analyses of pseudotachylyte from hole-B of Taiwan Chelungpu Fault Drilling Project (TCDP); Their implications for seismic slip behaviors during the 1999 Chi-Chi earthquake, *Tectonophysics*, *469*, 13–24.

Platt, J. D., J. W. Rudnicki, and J. R. Rice (2014), Stability and localization of rapid shear in fluid-saturated fault gouge: 2. Localized zone width and strength evolution, *J. Geophys. Res. Solid Earth*, *119*, 4334–4359, doi:10.1002/2013JB010711.

Platt, J. D., R. C. Viesca, and D. I. Garagash (2015), Steadily propagating slip pulses driven by thermal decomposition, *J. Geophys. Res. Solid Earth*, *120*, 6558–6591, doi:10.1002/2015JB012200.

Reches, Z., and D. A. Lockner (2010), Fault weakening and earthquake instability by power lubrication, *Nature*, *467*, 452–455.

Reynard, B. (2013), Serpentine in active subduction zones, *Lithos*, *178*, 171–185.

Pruess, K. (2011), GHGT-10: Modeling CO_2 leakage scenarios, including transitions between super- and sub-critical conditions, and phase change between liquid and gaseous CO_2, *Energy Proc.*, *4*, 3754–3761.

Rice, J. R. (2006), Heating and weakening of faults during earthquake slip, *J. Geophys. Res.*, *111*, B05311, doi:10.1029/2005JB004006.

Rice, J. R., J. W. Rudnicki, and J. D. Platt (2014), Stability and localization of rapid shear in fluid-saturated fault gouge: 1. Linearized stability analysis, *J. Geophys. Res. Solid Earth*, *119*, 4311–4333, doi:10.1002/2013JB010710.

Sakaguchi, A., A. Yanagihara, K. Ujiie, H. Tanaka, and M. Kameyama (2007), Thermal maturity of a fold-thrust belt based on vitrinite reflectance analysis in the Western Foothills complex, western Taiwan, *Tectonophysics*, *443*, 220–232.

Savage, H. M., P. J. Polissar, R. Sheppard, C. D. Rowe, and E. E. Brodsky (2014), Biomarkers heat up during earthquakes: New evidence of seismic slip in the rock record, *Geology*, *42*(2), 99–102.

Schleicher, A. M., A. Boles, and B. A. van der Pluijm (2015), Response of natural smectite to seismogenic heating and potential implications for the 2011 Tohoku earthquake in the Japan Trench, *Geology*, *43*, 755–758.

Scholz, C. H. (2002), *The Mechanics of Earthquakes and Faulting*, 2nd ed., pp. 53–100, Cambridge Univ. Press, Cambridge, U. K., and New York.

Segall, P., and A. M. Bradley (2012), The role of thermal pressurization and dilatancy in controlling the rate of fault slip, *J. Appl. Mech.*, *79*(3), doi:10.1115/1.4005896.

Segall, P., and J. R. Rice (1995), Dilatancy, compaction, and slip instability of a fluid-infiltrated fault, *J. Geopys. Res.*, *100*, 22,155–22,171, doi:10.1029/95JB02403.

Shi, J. X., and J. H. Wang (2011), A numerical investigation of transpiration cooling with liquid coolant phase change, *Transp. Porous Media*, *87*, 703–716.

Sone, H., and T. Shimamoto (2009), Frictional resistance of faults during accelerating and decelerating earthquake slip, *Nat. Geosci.*, *2*(10), 705–708.

Sulem, J., and V. Famin (2009), Thermal decomposition of carbonates in fault zones: Slip-weakening and temperature limiting effects, *J. Geophys. Res.*, *114*, B03309, doi:10.1029/2008JB006004.

Sulem, J., and I. Stefanou (2016), Thermal and chemical effects in shear and compaction bands, *Geomech. Energy Environ.*, *6*, 4–21.

Sulem, J., P. Lazar, and I. Vardoulakis (2007), Thermo-Poro-mechanical properties of clayey gouge and application to rapid fault shearing, *Int. J. Numer. Anal. Methods Geomech.*, *31*(3), 523–540.

Tanaka, H., W. M. Chen, C. Y. Wang, K. F. Ma, N. Urata, J. Mori, and M. Ando (2006), Frictional heat from faulting of the 1999 Chi-Chi, Taiwan earthquake, *Geophys. Res. Lett.*, *33*, L16316, doi:10.1029/2006GL026673.

Tanikawa, W., M. Sakaguchi, T. Hirono, W. Lin, W. Soh, and S.-R. Song (2009), Transport properties and dynamic processes in a fault zone from samples recovered from TCDP hole B of the Taiwan Chelungpu Fault Drilling Project, *Geochem. Geophys. Geosyst.*, *10*, Q04013, doi:10.1029/2008GC002269.

Tanikawa, W., T. Hirose, H. Mukoyoshi, O. Tadai, and W. Lin (2013), Fluid transport properties in sediments and their role in large slip near the surface of the plate boundary fault in the Japan Trench, *Earth Planet. Sci. Lett.*, *382*, 150–160.

Togo, T., and T. Shimamoto (2012), Energy partition for grain crushing in quartz gouge during subseismic to seismic fault motion: An experimental study, *J. Struct. Geol.*, *38*, 139–155.

Togo, T., T. Shimamoto, J.-J. Dong, C.-T. Lee, and C.-M. Yang (2014), Triggering and runaway processes of catastrophic Tsaoling landslide induced by the 1999 Taiwan Chi-Chi earthquake, as revealed by high-velocity friction experiments, *Geophys. Res. Lett.*, *41*, 1907–1915, doi:10.1002/2013GL059169.

Ujiie, K., and A. Tsutsumi (2010), High-velocity frictional properties of clay-rich fault gouge in a megasplay fault zone, Nanakai subduction zone, *Geophys. Res. Lett.*, *37*, L24310, doi:10.1029/2010GL046002.

Ujiie, K., et al. (2013), Low coseismic shear stress on the Tohoku-oki megathrust determined from laboratory experiments, *Science*, *342*, 1211–1214.

Urata, Y., K. Kuge, and Y. Kase (2013), Suppression of slip and rupture velocity increased by thermal pressurization: Effect of dilatancy, *J. Geophys. Res. Solid Earth*, *118*, 5827–5837, doi:10.1002/2013JB010640.

Vardoulakis, I. (2002), Dynamic thermo-poro-mechanical analysis of catastrophic landslides, *Geotechnique*, *52*, 157–171.

Voller, V. R., C. R. Swaminathan, and B. G. Thomas (1990), Fixed grid techniques for phase change problems: A review, *Int. J. Numer. Methods Eng.*, *30*, 875–898.

Wang, C. Y. (1997), A fixed-grid numerical algorithm for two-phase flow and heat transfer in porous media, *Numer. Heat Transfer B*, *32*(1), 85–105.

Wang, C. Y., and C. Beckermann (1993), A two-phase mixture model of liquid-gas flow heat transfer in capillary porous media–I: Formulation, *Int. J. Heat Mass Transfer*, *36*(11), 2747–2758.

Weatherley, D. K., and R. W. Henley (2013), Flash vaporization during earthquakes evidence by gold deposits, *Nat. Geosci.*, *6*, 294–298.

Wibberley, C. A. J., and T. Shimamoto (2005), Earthquake slip weakening and asperities explained by thermal pressurization, *Nature*, *436*, 689–692.

Wong, T.-F., S.-C. Ko, and D. L. Olgaard (1997), Generation and maintenance of pore pressure excess in a dehydrating system: 2. Theoretical analysis, *J. Geophys. Res.*, *102*(B1), 841–852, doi:10.1029/96JB02484.

Yang, T., M. J. Dekkers, and B. Zhang (2016), Seismic heating signatures in the Japan Trench subduction plate-boundary fault zone: Evidence from a preliminary rock magnetic "geothermometer", *Geophys. J. Int.*, *205*, 332–344.

Zoback, M., S. Hickman, and W. Ellsworth (2011), Scientific drilling into the San Andreas Fault zone: An overview of SAFOD's first five years, *Sci. Drill.*, *11*, 14–28.